New Journal of Physics
The open-access journal for physics

Turbulent collision efficiency of heavy particles relevant to cloud droplets

Lian-Ping Wang[1,3], Orlando Ayala[1], Bogdan Rosa[1] and Wojciech W Grabowski[2]

[1] 126 Spencer Laboratory, Department of Mechanical Engineering, University of Delaware, Newark, DE 19716-3140, USA
[2] Mesoscale and Microscale Meteorology Division, National Center for Atmospheric Research, PO Box 3000, Boulder, CO 80307-3000, USA
E-mail: lwang@udel.edu

New Journal of Physics **10** (2008) 075013 (41pp)
Received 17 December 2007
Published 31 July 2008
Online at http://www.njp.org/
doi:10.1088/1367-2630/10/7/075013

Abstract. The collision efficiency of sedimenting cloud droplets in a turbulent air flow is a key input parameter in predicting the growth of cloud droplets by collision–coalescence. In this study, turbulent collision efficiency was directly computed, using a hybrid direct numerical simulation (HDNS) approach (Ayala *et al* 2007 *J. Comput. Phys.* **225** 51–73). The HDNS results show that air turbulence enhances the collision efficiency partly due to the fact that aerodynamic interactions (AIs) become less effective in reducing the relative motion of droplets in the presence of background air turbulence. The level of increase in the collision efficiency depends on the flow dissipation rate and the droplet size ratio. For example, the collision efficiency between droplets of 18 and 20 μm in radii is increased by air turbulence (relative to the stagnant air case) by a factor of 4 and 1.6 at dissipation rates of 400 and 100 $\mathrm{cm}^2\,\mathrm{s}^{-3}$, respectively. The collision efficiency for self-collisions in a bidisperse turbulent suspension can be larger than one. Such an increase in self-collisions is related to the far-field many-body AI and depends on the volumetric concentration of droplets. The total turbulent enhancement agrees qualitatively with previous results, but differs on a quantitative level. In the case of cross-size collisions between 18 and 20 μm droplets, the total turbulent enhancement can be a factor of 7 and 2 at

[3] Author to whom any correspondence should be addressed.

dissipation rates of 400 and 100 $cm^2\ s^{-3}$, respectively. For intermediate size ratios ($0.2 < a_2/a_1 < 0.8$), the overall enhancement typically falls below 2. Scaling arguments show that the overall enhancement factor tends to peak at the two limiting cases of $a_2/a_1 \to 1$ and $a_2/a_1 \to 0$.

Contents

1. Introduction

Although the importance of air turbulence on rain formation was noted nearly 70 years ago [1], progress has been very slow in identifying and understanding the nature and quantitative importance of turbulence effects. This slow progress is due to the complexities associated with turbulence–droplet interactions and the long-time lack of reliable quantitative research tools. In the last 15 years, the availability of advanced computational research tools such as direct numerical simulations (DNS) of turbulent particle-laden flows has enabled researchers to advance physical understanding and theoretical treatment of turbulent collision rates of non-interacting (or 'point') particles [2]–[4]. The first attempts to include local droplet–droplet aerodynamic interaction (AI) within DNS were made recently by Wang *et al* [5] and Ayala *et al* [6]. Meanwhile, it remains a challenge to experimentally measure collision events of cloud droplets in a turbulent flow.

In warm (i.e. ice-free) clouds, growth of cloud droplets by collision–coalescence is a necessary step for precipitation formation. A collision–coalescence event occurs in three stages. Firstly, two droplets initially separated in space have to be brought together by their differential sedimentation and/or air turbulence. Secondly, when the two droplets are within about 50 times of the radius of the larger droplet, their trajectories can also be affected by the increasing local AI forces due to their own disturbance flows. If the approaching motion during the first stage is sufficiently strong, the droplets may overcome the barrier due to the local AI and touch each other, a collision is then said to occur. The last stage is when a collision event breaks the surface energy barrier to cause two separate droplet surfaces to coalesce into one, leading to the formation of a larger droplet. The first stage is usually referred to as the geometric collision. The percentage of geometric collisions that can overcome the AI barrier is termed as the collision efficiency. Finally, the percentage of collisions that can lead to coalescence is known as the coalescence efficiency. For cloud droplets less than 100 μm in radius, the ratio of inertial force to surface tension is rather small, it is commonly accepted that the coalescence efficiency is close to one [7]. For this reason, the study of collision–coalescence of cloud droplets concerns mainly the geometric collision rate and collision efficiency.

In two other contributions for this Focus Issue on Cloud Physics, we have studied the geometric collision rate of sedimenting cloud droplets in turbulent air, using both DNS and analytical methods. There it was shown that both the relative motion and local pair concentration can be moderately enhanced by air turbulence, leading to an enhanced geometric collision rate. The results on geometric collision rate serve as the necessary reference based on which the turbulent collision efficiency can then be properly specified [5].

In this paper, we focus on the collision efficiency of sedimenting cloud droplets in turbulent air. Qualitatively, turbulence is expected to alter the collision efficiency as the magnitude and orientation of droplet–droplet relative motion are affected by both the larger-scale background air turbulence and the AI forces at the droplet scale. However, quantitative study of turbulent collision efficiency is a very challenging task, since it requires a simultaneous representation of disturbance flows at the scale of the droplet size and air turbulent motion that occurs at scales at least one to two orders of magnitude larger. Furthermore, the usual definition of collision efficiency for sedimenting droplets in stagnant air, based on the relative grazing trajectory [7], is no longer applicable to turbulent collision–coalescence [5]. The very few existing studies on turbulent collision efficiency of cloud droplets [8]–[12] employed different kinematic definitions of turbulent collision efficiency, almost all of which are conceptually similar to the relative grazing trajectory. These definitions were used without direct validation using dynamic collision statistics. This problem along with different, inaccurate representations of the background air turbulence and different droplet-size combinations has generated somewhat controversial conclusions regarding the influence of turbulence on collision efficiency [5].

Our objective here is to quantify the collision efficiency using a dynamically validated formulation of collision efficiency [5] and a hybrid DNS (HDNS) approach [6]. Computation of kinematic properties of aerodynamically interacting droplets requires finite corrections due to the fact that droplets cannot overlap in space [5]. The basic idea of the HDNS approach is to combine DNS of the background air turbulence with an analytical representation of the disturbance flows induced by droplets. This hybrid approach provides a consistent quantitative tool for studying the combined effects of air turbulence and AIs on the motion and collisional interactions of cloud droplets. The disturbance flows are coupled with the background air turbulence through an approximate implementation of the no-slip boundary conditions on

each droplet. Dynamical features in three dimensions (3Ds) and on spatial scales ranging from a few tens of centimeters down to 10 μm are captured. Both the near-field and the far-field droplet–droplet AIs could be incorporated [13]. Limited preliminary results of turbulent collision efficiency using the HDNS approach have been reported in [13]. Here we will explore some of the parameter space relevant to cloud droplets, in terms of the droplet size and flow dissipation rate.

The paper will be organized as follows. In section 2, we will briefly review the necessary correction to the kinematic collision kernel formulation, developed by Wang *et al* [5], for aerodynamically interacting droplets. For completeness, a very brief description of the HDNS approach of Ayala *et al* [6] will be given in section 3. Results from the HDNS approach will be discussed in sections 4 through 6: these include kinematic pair statistics, collision kernel and collision efficiency. A preliminary theory of the radial relative velocity for aerodynamically interacting droplets will be developed and compared with the HDNS data. The effect of turbulence on the collision efficiency will be separated out from the effect of turbulence of the geometric collision kernel. The overall enhancement by turbulence will be compared with previously published results [10, 11]. Finally, conclusions are summarized in section 7.

2. Theoretical background

The theoretical formulation of collision rate and collision efficiency of aerodynamically interacting cloud droplets in turbulent air has been thoroughly treated in Wang *et al* [5]. It is, however, necessary to briefly review the formulation in order to properly analyze and interpret the HDNS results.

Consider a bidisperse system containing N_{p1} droplets of radius a_1 and N_{p2} droplets of radius a_2 in a volume V_B. It is assumed that $N_{p1} \gg 1$ and $N_{p2} \gg 1$. Following the convention, if $a_1 > a_2$, then the a_1-droplets are called the collecting droplets and the a_2-droplets are termed the collected droplets. The motion of each droplet is driven simultaneously by gravity, the undisturbed air turbulence and the disturbance flows of all other droplets. For example, an a_2-droplet can interact with any of the N_{p1} a_1-droplets and any of the other $(N_{p2}-1)$ a_2-droplets. A collision of this a_2-droplet with an a_1-droplet is called a cross-size collision, while a collision of this a_2-droplet with another a_2-droplet shall be termed as a_2–a_2 self-collision.

Therefore, there are three types of collisions: the a_1–a_2 cross-size collisions, a_1–a_1 self-collisions and a_2–a_2 self-collisions. The dynamic collision kernel for each type is a rate coefficient defined as

$$\Gamma_{12}^{\mathrm{D}} = \frac{\langle \dot{\mathcal{N}}_{12} \rangle}{n_1 n_2}, \quad \Gamma_{11}^{\mathrm{D}} = \frac{\langle \dot{\mathcal{N}}_{11} \rangle}{n_1^2/2}, \quad \Gamma_{22}^{\mathrm{D}} = \frac{\langle \dot{\mathcal{N}}_{22} \rangle}{n_2^2/2}, \tag{1}$$

where the subscripts 12, 11, 22 denote the types, $\langle \dot{\mathcal{N}} \rangle$ is the respective average number of collisions observed per unit time per unit volume, and the average number densities are defined as $n_1 \equiv N_{p1}/V_B$ and $n_2 \equiv N_{p2}/V_B$. In HDNS, all three types of collision events can be detected and so $\langle \dot{\mathcal{N}}_{12} \rangle$, $\langle \dot{\mathcal{N}}_{11} \rangle$, and $\langle \dot{\mathcal{N}}_{22} \rangle$ can be directly obtained. We shall refer to the collision kernels computed by equation (1) as the *dynamic* collision kernels (hence the superscript D).

When AIs are not considered, the average geometrical collision kernels can be described *kinematically* as

$$\Gamma_{12_{\mathrm{NAI}}}^{\mathrm{K}} = 2\pi R_{12}^2 \langle |w_{\mathrm{r},12}| \rangle_{\mathrm{NAI}} \, g_{12_{\mathrm{NAI}}}, \tag{2}$$

$$\Gamma^{\mathrm{K}}_{11_{\mathrm{NAI}}} = 2\pi R_{11}^2 \langle |w_{\mathrm{r},11}| \rangle_{\mathrm{NAI}}\, g_{11_{\mathrm{NAI}}}, \tag{3}$$

$$\Gamma^{\mathrm{K}}_{22_{\mathrm{NAI}}} = 2\pi R_{22}^2 \langle |w_{\mathrm{r},22}| \rangle_{\mathrm{NAI}}\, g_{22_{\mathrm{NAI}}}, \tag{4}$$

where the subscript 'NAI' denotes no AI, the geometric collision radii are $R_{12} = a_1 + a_2$, $R_{11} = 2a_1$, and $R_{22} = 2a_2$. Here, w_{r} is the radial component of the relative velocity $\mathbf{w}$ between two colliding droplets, namely, $w_{\mathrm{r}} = \mathbf{w} \cdot \mathbf{r}/r$, $\mathbf{r}$ is the relative separation vector, and $r = |\mathbf{r}|$. The factor g is the radial distribution function [2, 5] and measures the effect of preferential concentration on the local number density of colliding pairs. Both kinematic properties are evaluated at the respective collision radius.

For geometric collision, the above kinematic formulation has been shown to match the dynamic collision kernel, to within numerical uncertainty, in DNS [3]–[5]. Results from DNS of geometric collision kernel and related kinematic properties for sedimenting cloud droplets have been compiled in Franklin *et al* [12, 14] and Ayala *et al* [15, 16].

For the special case of geometric collision in stagnant air, we have

$$\Gamma^{\mathrm{g}}_{12} = \pi R^2 |v_{p1} - v_{p2}|, \tag{5}$$

since for this special case, $\langle |w_{\mathrm{r}}| \rangle_{\mathrm{NAI}} = 0.5|v_{p1} - v_{p2}|$ and $g_{12_{\mathrm{NAI}}} = 1$. Here v_{p1} and v_{p2} are the terminal velocities of the a_1- and a_2-droplets, respectively.

When AIs are not considered, each particle moves as if other particles were not present. Therefore, in previous DNS, particles were allowed to overlap in space and stay in the flow even when they had participated in collision events (so-called *ghost particles*). This was done mainly to keep the system truly stationary. When AIs are taken into account, droplets can no longer overlap in space as this becomes unphysical. This also implies that droplets cannot penetrate through each other. In our HDNS approach, a non-overlap requirement is incorporated. Namely, every time a collision event occurs, we remove the pair from their current locations and, at the same time, add another two droplets having the same material properties as the pair just removed, back to the computational domain. The locations of the two added droplets are randomly chosen and care is taken to make sure that they do not overlap with any other droplets in the system. Their velocities are set to their terminal velocity plus the local fluid velocity. They are then tracked by solving their equation of motion just like all other droplets. In this manner, the total number of droplets remains the same and no droplet overlaps with any other droplet at the beginning of a time step. The above treatment mimics most closely the real situation of stochastic collision–coalescence of cloud droplets, since coalescence of two droplets will remove these droplets from their own size groups while coalescence of smaller droplets can introduce new droplets to these size groups.

Wang *et al* [5] showed that the same kinematic formulation can be applied to the collision kernel of aerodynamically interacting droplets after a correction due to the above non-overlap requirement is applied to the kinematic properties. Specifically, they proposed that the kinematic properties for aerodynamically interacting droplets should be computed as follows:

$$g_{12_{\mathrm{AI}}} = g_{12}^{\mathrm{HDNS}} / G_{12}(r_1, r_2), \tag{6}$$

$$\langle |w_{\mathrm{r},12}| \rangle_{\mathrm{AI}} = \langle |w_{\mathrm{r},12}| \rangle^{\mathrm{HDNS}} \times \frac{G_{12}(r_1, r_2)}{1 - 1.5R^2(r_2 - r_1)/(r_2^3 - r_1^3)}, \tag{7}$$

where r_1 and r_2 are the inner and outer radii of a narrow spherical shell used to collect pairs for computing the kinematic properties, they are typically set to $r_1 = R_{12}$ and $r_2 = 1.02R_{12}$ for

the evaluation of the kinematic collision kernel [5]. The superscript 'HDNS' denotes values computed from HDNS under the non-overlap condition. Namely, g_{12}^{HDNS} represents the ratio of the actual pair density realized in HDNS to the expected pair density corresponding to a uniform droplet distribution, and $\langle|w_{\mathrm{r},12}|\rangle^{\mathrm{HDNS}}$ is the average radial relative velocity based on the actual detected pairs in HDNS. The function $G_{12}(r_1, r_2)$ is specified as

$$G_{12}(r_1, r_2) = 0.5 + 0.5[(r_2^2 - R_{12}^2)^{3/2} - (r_1^2 - R_{12}^2)^{3/2}]/(r_2^3 - r_1^3). \tag{8}$$

The correction or the re-scaling factors depend on the shell thickness. It is assumed that the results obtained by equations (6) and (7) are relatively insensitive to the exact thickness, $(r_2 - r_1)$, used if the thickness is made very small. Similar correction or rescaling can be applied to self-collisions of aerodynamically-interacting droplets.

The turbulent collision efficiency can now be defined as the ratio of collision kernel with AI to the geometric collision kernel (i.e. the reference collision kernel) when the AI is not activated:

$$E_{12}^{\mathrm{D}} = \frac{\Gamma_{12_{\mathrm{AI}}}^{\mathrm{D}}}{\Gamma_{12_{\mathrm{NAI}}}^{\mathrm{D}}}. \tag{9}$$

Alternatively, since the kinematic formulation applies to both cases with and without AI, we would have

$$E_{12}^{\mathrm{K}} = \frac{\Gamma_{12_{\mathrm{AI}}}^{\mathrm{K}}}{\Gamma_{12_{\mathrm{NAI}}}^{\mathrm{K}}} = \frac{\langle|w_{\mathrm{r}}, 12|\rangle_{\mathrm{AI}}}{\langle|w_{\mathrm{r}}, 12|\rangle_{\mathrm{NAI}}} \times \frac{g_{12_{\mathrm{AI}}}}{g_{12_{\mathrm{NAI}}}}, \tag{10}$$

where it is implied that all the kinematic properties are evaluated at $r = R_{12}$. This second method indicates that if the effects of AIs on the relative velocity and pair distribution density could be quantified either theoretically or numerically, a parameterization can be developed for the turbulent collision efficiency. The turbulent collision efficiency for self-collisions can be similarly defined.

In the atmospheric sciences community, the collision kernel is often written relative to the reference case of aerodynamical–gravitational coagulation. As long as the collisions of droplets of unequal sizes are considered, we can write

$$\Gamma_{12} = \eta_{\mathrm{E}}\eta_{\mathrm{G}}E_{12}^{\mathrm{g}}\Gamma_{12}^{\mathrm{g}}, \tag{11}$$

where Γ_{12}^{g} is the geometrical gravitational collision kernel given by equation (5), E_{12}^{g} is the collision efficiency for the aerodynamical–gravitational problem and may be computed as $E_{12}^{\mathrm{g}} = y_{\mathrm{c}}^2/R_{12}^2$, where y_{c} is the far-field, off-center horizontal separation of the relative grazing trajectory [5, 7]. η_{G} represents an enhancement factor due to turbulence on the geometric collision kernel and is defined as

$$\eta_{\mathrm{G}} = \frac{\Gamma_{12_{\mathrm{NAI}}}}{\Gamma_{12}^{\mathrm{g}}}. \tag{12}$$

η_{E} represents an enhancement factor due to turbulence on the collision efficiency and is defined as

$$\eta_{\mathrm{E}} = \frac{E_{12}}{E_{12}^{\mathrm{g}}}. \tag{13}$$

In the literature, the turbulent collision efficiency was sometime not properly defined (e.g. see table 1 in [5]), often leading to the product of the two enhancement factors, $(\eta_{\mathrm{G}}\eta_{\mathrm{E}})$, being incorrectly interpreted as the effect of turbulence on the collision efficiency. The enhancement factor η_{G} was discussed in our parallel contribution to this focus issue [15]. This paper will mainly focus on the enhancement factor η_{E} on the collision efficiency.

3. HDNS

In this section, we present a condensed version of a description of the HDNS approach focusing on the physical issues, without discussion of numerical implementation issues. The latter can be found in [6]. The goal of HDNS was to include droplet–droplet AIs in DNS of droplet-laden turbulent flows. It was assumed that the disturbance flows due to droplets are very localized in space and there is a sufficient length-scale separation between the droplet size and the Kolmogorov scale of the undisturbed turbulent flow. Each droplet moves according to a composite flow consisting of the background air turbulence and a superposition of disturbance flows due to all other droplets in the system. The relatively larger-scale, background air turbulence is fully resolved by the usual DNS using a pseudospectral method, while the droplet-scale disturbance flows are represented in terms of analytical Stokes flows. The magnitude of each analytical disturbance flow is adjusted so that the no-slip condition on the surface of each droplet is satisfied on average. This logical step significantly improves the accuracy of the method in treating the AI, yet the background air turbulence is naturally coupled with the disturbance flows. The computation of disturbance flows requires a solution of a large linear system, which is performed by a Gauss–Seidel procedure [6].

The flow field experienced by a droplet is the combination of the background air turbulence $\mathbf{U}(\mathbf{x}, t)$ and the combined disturbance flow $\tilde{\mathbf{u}}(\mathbf{x}, t)$ but with its own disturbance flow removed. The combined flow field, $\tilde{\mathbf{U}}(\mathbf{x}, t) \equiv \mathbf{U}(\mathbf{x}, t) + \tilde{\mathbf{u}}(\mathbf{x}, t)$, is referred to as the composite flow field. The key element is the proper and optimal specification of $\tilde{\mathbf{u}}(\mathbf{x}, t)$, provided that $\mathbf{U}(\mathbf{x}, t)$ is known.

The disturbance flow field in a system containing $N_p = N_{p1} + N_{p2}$ small droplets is written as

$$\tilde{\mathbf{u}}(\mathbf{x}, t) = \sum_{k=1}^{N_p} \mathbf{u}_S \left(\mathbf{r}^{(k)}; a^{(k)}, \mathbf{V}^{(k)} - \mathbf{U}(\mathbf{Y}^{(k)}, t) - \mathbf{u}^{(k)} \right), \tag{14}$$

where

$$\mathbf{u}_S(\mathbf{r}^{(k)}; a^{(k)}, \mathbf{V_p}^{(k)}) \equiv \left[\frac{3}{4}\frac{a^{(k)}}{r^{(k)}} - \frac{3}{4}\left(\frac{a^{(k)}}{r^{(k)}}\right)^3 \right] \frac{\mathbf{r}^{(k)}}{(r^{(k)})^2} (\mathbf{V_p}^{(k)} \cdot \mathbf{r}^{(k)}) + \left[\frac{3}{4}\frac{a^{(k)}}{r^{(k)}} + \frac{1}{4}\left(\frac{a^{(k)}}{r^{(k)}}\right)^3 \right] \mathbf{V_p}^{(k)} \tag{15}$$

represents the Stokes disturbance flow due to the kth droplet of radius $a^{(k)}$ moving at velocity $\mathbf{V_p}^{(k)}$ in an otherwise quiescent fluid, and $\mathbf{r}^{(k)} \equiv \mathbf{x} - \mathbf{Y}^{(k)}$. Here $\mathbf{Y}^{(k)}$ is the instantaneous location of the kth droplet. Equation (15) is based on a single isolated particle and represents a combination of a Stokeslet and a potential dipole flow [17].

Equation (14) contains explicitly the disturbance flow velocity $\mathbf{u}^{(k)}$ at the location $\mathbf{Y}^{(k)}$ of the kth droplet, due to all other droplets in the system. In equation (14), the combination $[\mathbf{V}^{(k)} - \mathbf{U}(\mathbf{Y}^{(k)}, t) - \mathbf{u}^{(k)}]$ represents the relative velocity between the kth droplet and the composite flow $\tilde{\mathbf{U}}(\mathbf{x}, \mathbf{t})$, excluding the disturbance flow due to the kth droplet itself. Namely, $\mathbf{u}^{(k)}$ represents the disturbance flow velocity due to all droplets except the kth droplet, at the location of the kth droplet. $\mathbf{u}^{(k)}$ is determined by applying the center-point approximation [5] to the boundary conditions $\tilde{\mathbf{U}}(|r^{(k)}| = a^{(k)}, t) = \mathbf{V}^{(k)}$, yielding

$$\mathbf{u}^{(k)} = \underbrace{\sum_{m=1}^{N_p}}_{m \neq k} \mathbf{u}_S \left(\mathbf{d}^{(mk)}; a^{(m)}, \mathbf{V}^{(m)} - \mathbf{U}(\mathbf{Y}^{(m)}, t) - \mathbf{u}^{(m)} \right), \qquad \text{for} \quad k = 1, 2, \ldots, N_p, \tag{16}$$

where $\mathbf{d}^{(mk)} \equiv \mathbf{Y}^{(k)} - \mathbf{Y}^{(m)}$. Therefore, $\mathbf{u}^{(k)}$ is a function of the background flow field and, the instantaneous locations and velocities of *all* droplets. Equation (16) implies that each disturbance flow velocity component at the location of the kth droplet will depend on all the disturbance flow velocity components of all other droplets. Equation (16) is a linear system of dimension $3N_p$.

Since the Stokes flow induced by the mth droplet in equation (16) decays with $\mathbf{d}^{(mk)}$ as $a^{(m)}/d^{(mk)}$, as an approximation and also for computational efficiency, we truncate the right hand side of equation (16) at $d^{(mk)}/a^{(m)} = H$, or only contributions to the summation from neighboring droplets with $d^{(mk)}/a^{(m)} \leqslant H$ are considered. Physically, the dimensionless truncation radius H should be made on the order of $(Re_p)^{-1}$ as the far-field disturbance flow can be better modeled by the Oseen's equation [17, 18], where Re_p is the droplet Reynolds number. Here we simply set H to be $50a^{(k)}$, a value large enough so that the resulting collision kernel does not depend on H [6].

The drag force acting on the kth particle due to the interactions with the turbulent flow field and the disturbance flow field can be rigorously shown to be [5]

$$\mathbf{D}^{(k)}(t) = -6\pi\mu a_k \left[\mathbf{V}^{(k)}(t) - \left(\mathbf{U}(\mathbf{Y}^{(k)}(t), t) + \mathbf{u}^{(k)}\right)\right]. \tag{17}$$

Therefore, the equation of motion of any given droplet 'k' is

$$\frac{\mathrm{d}\mathbf{V}^{(k)}(t)}{\mathrm{d}t} = -\frac{\mathbf{V}^{(k)}(t) - \left(\mathbf{U}(\mathbf{Y}^{(k)}(t), t) + \mathbf{u}^{(k)}\right)}{\tau_{\mathrm{p}}^{(k)}} + \mathbf{g}, \tag{18}$$

$$\frac{\mathrm{d}\mathbf{Y}^{(k)}(t)}{\mathrm{d}t} = \mathbf{V}^{(k)}(t), \tag{19}$$

where $\tau_p^{(k)} = 2\rho_p(a^{(k)})^2/(9\mu)$ is the droplet inertial response time, ρ_p is the droplet density, and μ is the air dynamic viscosity. Without the disturbance flow, there are two important governing parameters for the motion of any particle [19]: the first is the Stokes number defined as $St \equiv \tau_{\mathrm{p}}/\tau_{\mathrm{k}}$, the ratio of particle response time to flow Kolmogorov time τ_{k}; the second is the nondimensional terminal velocity defined as $S_{\mathrm{v}} \equiv (\tau_{\mathrm{p}}|\mathbf{g}|)/v_{\mathrm{k}}$, the ratio of particle terminal velocity to the flow Kolmogorov velocity v_{k}.

In both equations (17) and (18), the disturbance flow velocity experienced by each particle, $\mathbf{u}^{(k)}$, plays the central role. The disturbance flow velocities of all droplets together naturally incorporate the droplet–droplet AIs when droplets are in close proximity on the scale of droplet diameter.

The background air flow was generated by solving the full 3D, time-dependent Navier–Stokes equation using a pseudospectral method [19]. The background flow was simulated in two stages. The first stage was to generate the flow from rest by the random forcing term $\mathbf{f}(\mathbf{x}, t)$ which is nonzero only for a few modes at low wave numbers. We evolve the flow from $t = 0$ to at least $t = 9T_{\mathrm{e}}$ (T_{e} is the large-eddy turnover time) to ensure it has reached a statistically stationary state. Such a flow state is characterized by a balance, on average, between the rate of energy introduced by $\mathbf{f}(\mathbf{x}, t)$ and the rate of viscous energy dissipation. The small-scale features of the flow are characterized by the Kolmogorov scales defined based on the viscous dissipation rate and kinematic viscosity; namely, the Kolmogorov length, time and velocity scale are

$$\eta = (\nu^3/\epsilon)^{1/4}; \quad \tau_{\mathrm{k}} = (\nu/\epsilon)^{1/2}; \quad v_{\mathrm{k}} = (\nu\epsilon)^{1/4}.$$

Table 1. DNS flow parameters and characteristics.

	$100\ \mathrm{cm^2\ s^{-3}}$		$400\ \mathrm{cm^2\ s^{-3}}$	
	64^3	128^3	64^3	128^3
u' ($\mathrm{cm\ s^{-1}}$)	6.768	8.779	9.572	12.416
L_f (cm)	3.119	6.839	2.206	4.837
$\langle (Du/Dt)^2 \rangle$	3.752×10^3	5.010×10^3	3.002×10^4	4.008×10^4
λ_D	0.4754	0.5012	0.3361	0.3544
T_e (s)	0.458	0.771	0.229	0.385
v_k ($\mathrm{cm\ s^{-1}}$)	2.031	2.031	2.872	2.872
τ_k (s)	0.0412	0.0412	0.0206	0.0206
η (cm)	0.0837	0.0837	0.0592	0.0592
λ (cm)	1.081	1.402	0.764	0.991
R_λ	43.037	72.408	43.037	72.408
Box size (cm)	11.840	23.680	8.384	16.768
Δx (cm)	0.185	0.185	0.131	0.131
$\mathrm{d}t \times 10^3$ (s)	1.110	0.898	0.555	0.449
CFL	0.2831	0.301	0.2831	0.301
$k_{\max}\eta$	1.3619	1.3826	1.3619	1.3826

The large-scale features may be characterized by the rms fluctuation velocity or flow Taylor-microscale Reynolds number

$$u' \equiv \sqrt{\frac{\langle \mathbf{U} \cdot \mathbf{U} \rangle}{3}}, \qquad R_\lambda = \sqrt{15} \left(\frac{u'}{v_k} \right)^2 .$$

In the second stage, droplets were introduced into the flow and transported by the turbulence. At this stage, flow parameters were calculated and droplet statistics were accumulated. Two flow dissipation rates were considered in the simulations. Table 1 lists the simulated flow parameters and properties: the component rms fluctuating velocity u', integral length scale L_f, fluid acceleration variance $\langle (Du/Dt)^2 \rangle$, longitudinal Taylor-type microscale of fluid acceleration λ_D, eddy turnover time T_e, Kolmogorov velocity scale v_k, Kolmogorov timescale τ_k, Kolmogorov length scale η, Taylor microscale λ, Taylor microscale Reynolds number R_λ, size of the cubic box flow domain, grid spacing Δx, and flow time step size $\mathrm{d}t$. The time step was chosen to ensure that the CFL number was 0.3 or less for numerical stability and accuracy. The spatial resolution of the simulations was monitored by the value $k_{\max}\eta$ which should be greater than unity for the smallest scales of flow to be resolved. We note that the range of scales of turbulent motion is necessarily limited in our DNS, so the relative motion of large droplets considered in this study (50 μm) may be affected by large-scale eddies not realized in our DNS.

Once the background turbulent flow field is known, the air velocity at the location of a droplet, $\mathbf{U}(\mathbf{Y}^{(k)}, t)$, is interpolated. The disturbance flow velocities $\mathbf{u}^{(k)}$ can then be solved from equation (16). The velocities and locations of all droplets are advanced using equations (18) and (19). A fourth-order Adams–Bashforth method was used to numerically integrate these two differential equations.

The droplets were introduced randomly into the computational domain when the background turbulent flow had reached the statistically stationary stage. The initial velocity

condition was set equal to the local fluid velocity plus the terminal velocity of the droplet v_p. Collision-related statistics were accumulated to obtain running averages only after a time about $3 \times \max(\tau_{p1}, \tau_{p2})$ in order to minimize any effect of the initial conditions.

Dynamic collision detection was based on the efficient cell-index method and the concept of linked lists [20]. A collision detection grid was properly chosen so that all collision events were counted and, at the same time, no time was wasted on processing pairs of large separations. A cross-size collision event was counted during the time step if $|\mathbf{r}(t)| \equiv |\mathbf{Y}^{(2)}(t) - \mathbf{Y}^{(1)}(t)|$ became less or equal to $(a_1 + a_2)$. In the current approach, the lubrication force at very small separations is underestimated so two droplets can overlap, and when this occurs a coalescence event is assumed. While we were primarily interested in the 1–2 collision events, self-collisions (1–1 and 2–2) were also detected.

A variety of kinematic statistics related to individual droplets and droplet–droplet interactions were computed, including the mean velocity and velocity fluctuation of droplets, the radial relative velocity, and the radial distribution function. These were processed for the cross-size (12) pairs and like-size (11 and 22) pairs.

In summary, at each time step, the following procedure was implemented to advance the turbulent suspension system:

1. advance the undisturbed air turbulence $\mathbf{U}(\mathbf{x}, t)$;
2. interpolate the undisturbed air velocities at the locations of the droplets, $\mathbf{U}(\mathbf{Y}^{(k)}, t)$;
3. solve the disturbance flow velocity $\mathbf{u}^{(k)}$ experienced by each droplet;
4. advance the velocities and locations of the droplets;
5. detect droplet–droplet collision events and calculate relevant kinematic and dynamic properties.

4. General results on collision kernel

Since the disturbance flows of all droplets were included in the HDNS approach, the a_2–a_2 self-collisions could be affected by the presence of a_1-droplets and a_1–a_1 self-collisions could be affected by the presence of a_2-droplets [13]. It is important to note that our HDNS approach contains two important aspects that usually were not included in previous studies of gravitational collisions in stagnant air. The first concerns the effect of multi-body AIs in the system. For example, self-collisions are possible due to multi-body AI even in stagnant air, as the cumulative multi-body AIs cause finite velocity fluctuations of droplets—a phenomenon well known in the suspension mechanics (e.g. [21]). The second aspect is the observation that both self-collisions and cross-size collisions may depend on the complete details of the bidisperse system including the concentrations of a_1-size and a_2-size droplets, as the carrier flow is shared by the droplets each of which contributes and responds to the disturbance flow field. This would not be the case if AI were not considered, e.g. a_2–a_2 self-collisions would not depend on the presence of droplets of other sizes without AI.

With the above clarifications, we shall focus on the collisional interactions with collecting droplets of radii 20, 30 and 50 μm in a bidisperse system. Self-collisions of droplets in these bidisperse systems will also be studied.

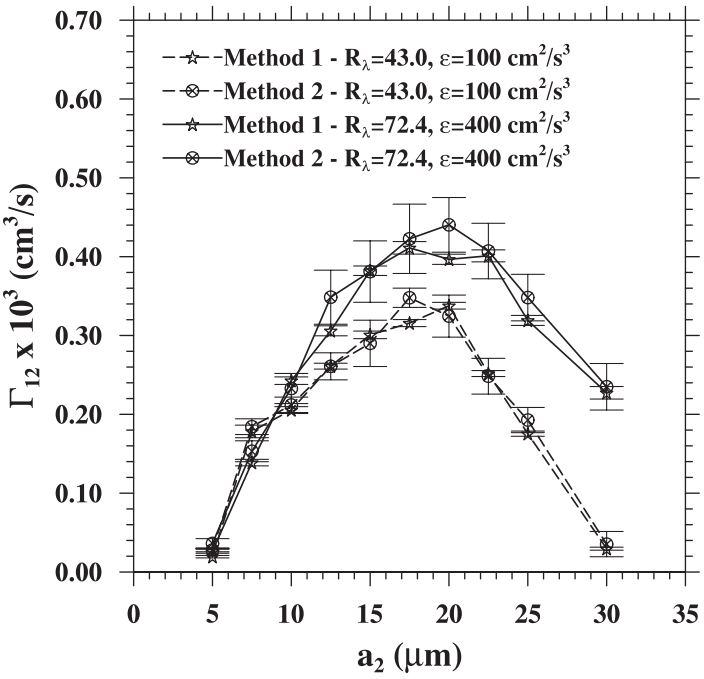

Figure 1. Comparison of the dynamic collision kernel (method 1) with the kinematic kernel (method 2). The collecting droplets are 30 μm in radius. In the self-collision case (30 μm–30 μm), the radius of the second-group droplets was 25 μm.

4.1. Kinematic versus dynamic collision kernel

In figure 1, we compare the dynamic collision kernel (Γ_{12}^{D}, method 1) with the kinematic collision kernel (Γ_{12}^{K}, method 2) for a bidisperse system of aerodynamically interacting droplets with the collecting droplets 30 μm in radius. The corrections to the kinematic properties discussed in section 2 have already been applied to process the kinematic collision kernels. The error bars represent the statistical uncertainties at one standard deviation. It is noted that the uncertainties for the kinematic kernel are much larger than those for the dynamic kernel, as both the uncertainties in the radial relative velocity and the radial distribution function must be combined in order to evaluate the uncertainty for the kinematic kernel. Furthermore, the pairs have to be kept near contact with $r_1 = R$ and $r_2 = 1.025R$ for a good representation of the at-contact kinematics, such a thin spherical shell limits the number of pairs realizable in HDNS. Nevertheless, the corrected kinematic kernels agree with the dynamic kernels for all the cases shown in figure 1 within the estimated statistical uncertainties. This confirms the observation in Wang *et al* [5] that the corrected kinematic kernel is consistent with the dynamic collision kernel for aerodynamically interacting droplets.

4.2. Collision kernel with AI versus geometric collision kernel

To illustrate the effect of AI on the collision kernel, we plot the dynamic collision kernels in figure 2 for cross-size and self-collisions in bidisperse systems with $a_1 = 30\,\mu$m, and also the results of the corresponding geometric collision kernels. The number of droplets followed

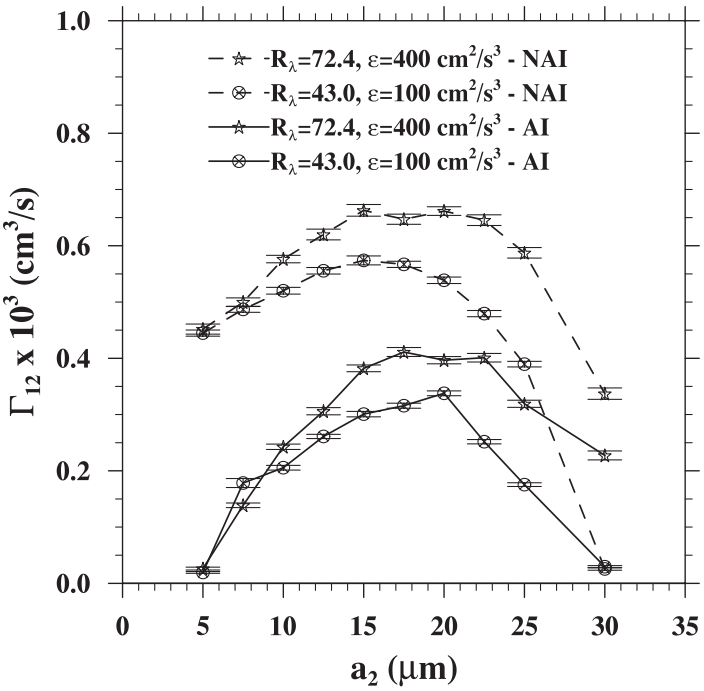

Figure 2. Comparison of the collision kernels with and without droplet–droplet AIs. The collecting droplets are 30 μm in radius. In the self-collision case (30 μm–30 μm), the radius of the second-group droplets was 25 μm.

in HDNS varied for different bidisperse systems. For instance, two bidisperse systems in a turbulent flow at $R_\lambda = 43.0$ and $\epsilon = 100\,\mathrm{cm^2\,s^{-3}}$ have the following numbers of droplets: for $a_2 = 5\,\mu$m, $N_{p1} = N_{p2} = 250\,000$; while for $a_2 = 25\mu$m, $N_{p1} = N_{p2} = 80\,000$. The total liquid water contents for these two cases are 17.28 and 10.32 $\mathrm{g\,m^{-3}}$. As expected, the AIs reduce the rate of collisions relative to the geometric collision case. This mainly results from an attenuation of the radial relative velocity. The reduction is more pronounced for smaller a_2/a_1 as an a_2-size droplet is increasingly affected by the disturbance flow of an a_1-droplet when the pair are in close proximity. An interesting observation is that the collision kernel for a_1–a_1 self-collisions with AI can be larger than that of geometric self-collisions. This aspect will be discussed in the next section.

5. Results for self-collisions

In order to understand the observed increase in the collision kernel for self-collisions, we shall first examine separately the effects of AIs on the radial relative velocity and the radial distribution function.

Recall that a_1–a_1 self-collisions were studied with the presence of a_2-droplets. Figure 3 shows the droplet number density n_1 of a_1-droplets ($n_1 = N_{p1}/V_{\mathrm{box}}$) employed during simulations with $a_1 = 30\mu$m. The number density of a_2-droplets was always set to be the same as that of the a_1-droplets, which is likely not the case in real clouds. Similar number densities were used for collecting droplets of 20 or 50 μm in radius. Note that larger number densities were sometimes used for the cases of small a_2/a_1 to increase the number of collisions

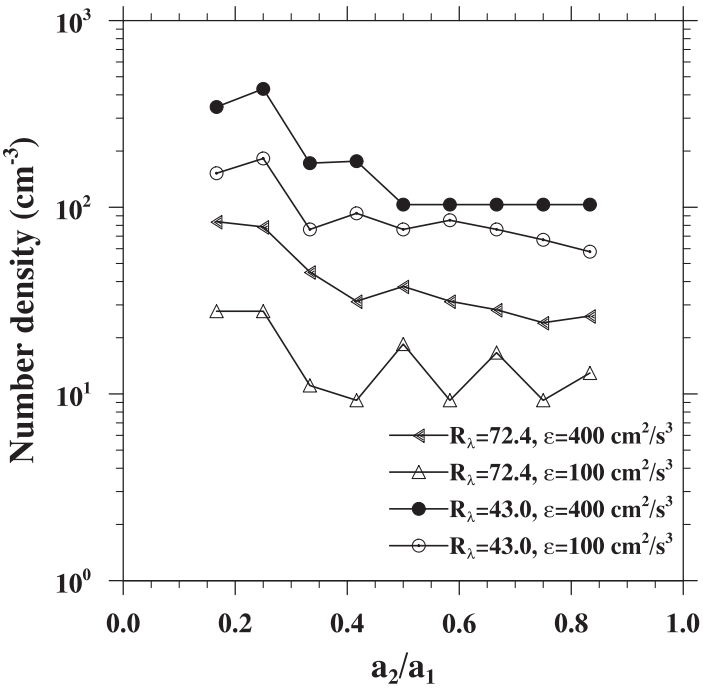

Figure 3. Droplet number densities for each droplet size in HDNS simulations involving $a_1 = 30\,\mu$m.

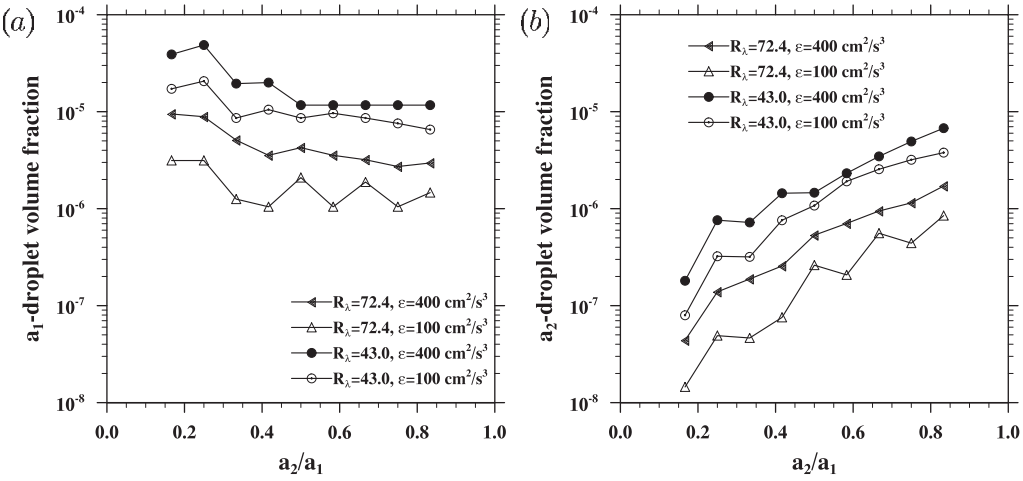

Figure 4. Volume fractions in HDNS simulations involving $a_1 = 30\,\mu$m: (a) a_1-droplets and (b) a_2-droplets.

for controlled statistical uncertainty [6]. Figure 4 shows the volume fractions of the two size groups for the simulations where the collecting droplet radius was 30 μm. In some small a_2/a_1 cases, the volume fraction was one order of magnitude larger than what is present in real clouds (typically $\phi \sim 10^{-6}$). From the figure, the total liquid water content (LWC) can be found by $\mathrm{LWC} = (\phi_1 + \phi_2)\rho_w$ and is in the range of 1–50 g m^{-3}.

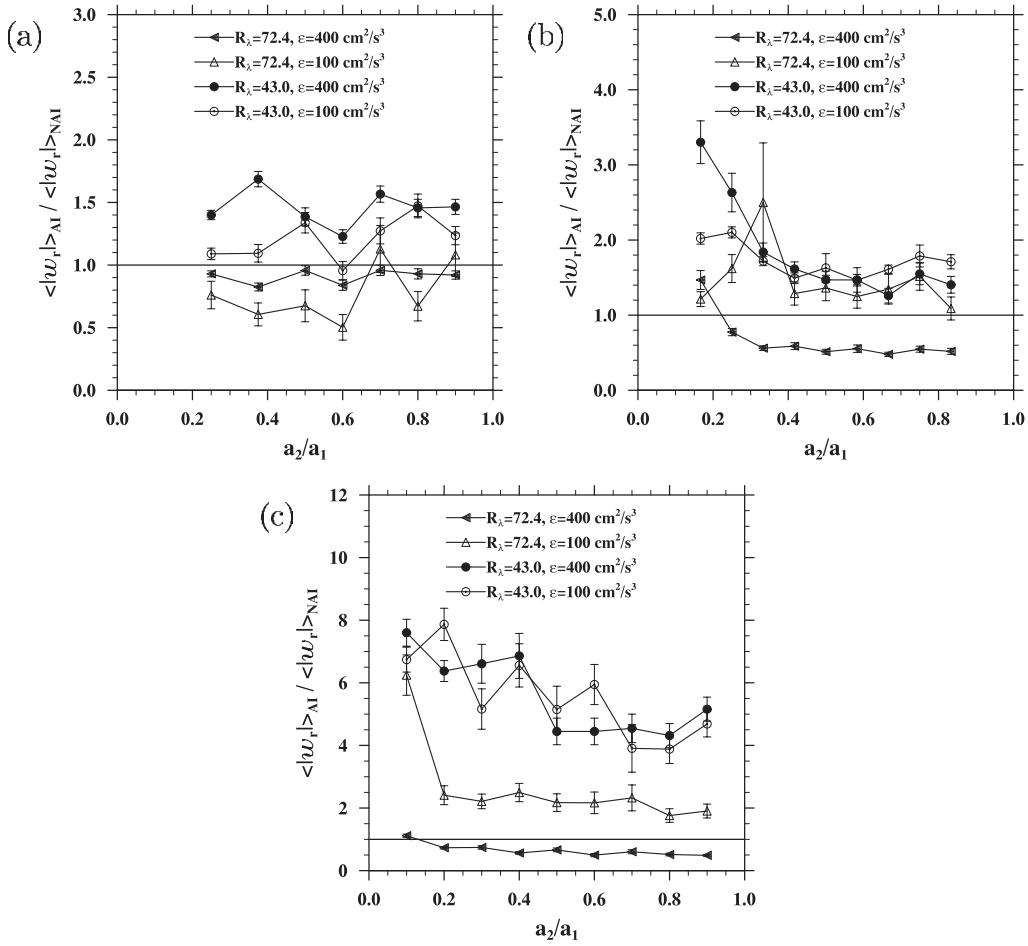

Figure 5. Ratio of the radial relative velocity with AI to that corresponding to geometric collisions for a_1–a_1 self-collisions. (a) $a_1 = 20\,\mu$m, (b) $a_1 = 30\,\mu$m and (c) $a_1 = 50\,\mu$m.

5.1. Radial relative velocity

Figure 5 shows the ratio of the radial relative velocity with AI to that corresponding to geometric self-collisions of collecting droplets for the three collecting-droplet sizes. Note that $\langle|w_r|\rangle_{NAI}$ is independent of a_2/a_1. The dependence of $\langle|w_r|\rangle_{AI}$ on a_2/a_1 physically represents the cumulative effect of the disturbance flows of all other droplets on the motion of an a_1-droplet (related to the changing volumetric concentrations used). For the case of $a_1 = 20\,\mu$m (figure 5(a)), contrary to the expected reduction of relative velocity, we observe an increase in the a_1–a_1 radial relative velocity at $R_\lambda = 43.0$ when AI is included. This result could be due to the large droplet volume concentrations used in those cases (from $\phi = 1.44 \times 10^{-5}$ to 5.76×10^{-6}). Stokes disturbance flows decay slowly with distance and the cumulative effect of many-body interactions does not diminish at large inter-droplet separations [13, 21]. The level of velocity fluctuation due to these cumulative many-body interactions increases with droplet number density (or droplet volume fraction), as shown by the relative location of the curves in figure 5(a) when compared to that shown in figure 3.

In general, there are two different mechanisms by which that AI can alter the radial relative velocity. The first mechanism is related to the near-field pair interaction, with center-to-center separation less than, say, $5R$. This near-field pair interaction occurs for all colliding pairs and for some other pairs that are forced to move toward each other by the background air turbulence or differential sedimentation. These near-contact pairs experience large viscous force in the radial direction and, as a result, their relative motion in the radial direction is reduced. Therefore, this near-field pair interaction causes a reduction of radial relative velocity.

The second mechanism is the cumulative far-field many-body interaction. A droplet in a suspension moves in response to the disturbance flows of all other droplets in the system. For our HDNS, if the droplet is located within the truncation radius (typically $50a^{(k)}$) of the kth droplet, its motion is affected by the kth droplet. There are many such kth droplets surrounding the droplet being considered, and cumulatively they induce a fluctuating motion on the droplet [13, 21]. This far-field interaction can actually increase the radial relative motion. An example is the motion due to the many-body AI in a suspension without background air turbulence. In such a simple case, droplets move along fluctuating paths and each pair can have relative motion in all directions. It is important to point out that this far-field interaction was usually not considered in the past when the aerodynamic-gravitational collision problem was studied.

The effect of this far-field interaction depends on the nature of the disturbance flows and the overall volumetric concentration of droplets in the suspension. For Stokes disturbance flows, the fluctuating motion caused by this far-field interaction is roughly proportional to the concentrations of the two groups of particles in the bidisperse suspension [13]. The level of fluctuations also depends on the truncation radius as the cumulative effect of disturbance flows does not decay with distance [13]. At very low concentrations, the near-field interaction dominates so the radial relative velocity is reduced by AI. However, at finite concentrations, the far-field many-body interaction can dominate the effect of AI leading to an increase of radial relative velocity. This is clearly observed for all values of a_1 considered in figure 5. The level of increase in the radial relative velocity is larger for larger a_1, for all the a_2/a_1 ratios considered.

This can be better understood in terms of the ratio of λ_{11}/a_1, where λ_{11} is the mean separation distance in the size-1 suspension and is defined as $\lambda_{11} = (V_{\text{box}}/N_{p1})^{1/3}$. In figure 6, we show this mean separation distance in the size-1 suspension for simulations involving $a_1 = 30\ \mu$m. Figure 6 shows that the mean separation distance is comparable to the AI truncation radius, so the far-field many-body interaction cannot be neglected. This effect is stronger when λ_{11}/a_1 is smaller, which is qualitatively confirmed by comparing figure 5(b) with figure 6.

Due to the effect of AI on both the direction and magnitude of the droplet relative velocities, the level of non-uniform pair concentration can also be affected by AI, as explained in [22]. Figure 7 shows the ratio of the radial distribution function with droplet–droplet AI to that corresponding to the geometric collision case. The first observation is that the modification of the droplet pair concentration by AI appears to be inversely related to the relative change of the radial relative velocity by AI. This inverse relationship can be qualitatively explained as follows. If the radial relative velocity is reduced by AI, it takes a longer time to separate the pair. In such a case, the RDF is likely to be increased. On the other hand, an increase in the average radial relative motion implies that the pair spend less time in close proximity and as such the RDF will be less. The two modifications on the relative motion and RDF are not exactly at inverse proportion to one another. The net effect will be the deviation of collision efficiency from one which is discussed next.

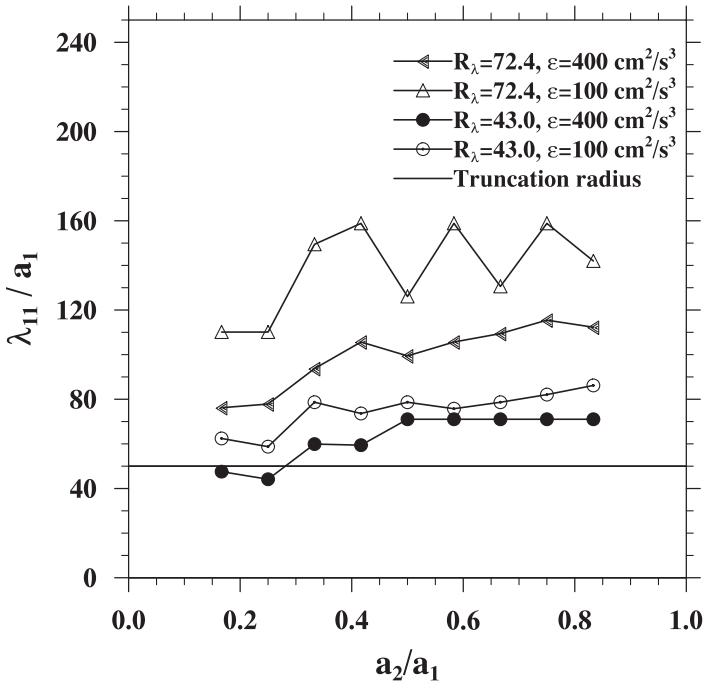

Figure 6. Mean separation distance in the size-1 suspension for simulations involving $a_1 = 30\,\mu$m. The horizontal line denotes the AI truncation radius.

5.2. Collision efficiency

Figure 8 shows the turbulent collision efficiency for a_1–a_1 self-collisions based on the dynamic kernel. This is essentially the product of the two ratios shown in figures 5 and 7 according to the kinematic description. The collision efficiencies for $20\,\mu$m droplets are smaller than one. For $30\,\mu$m droplets in a turbulent flow at $R_\lambda = 72.4$ and $\epsilon = 400\,\text{cm}^2\,\text{s}^{-3}$, however, the collision efficiency can become larger than one. This seems to be due to the enhanced clustering overtaking the reduction in the radial relative velocity. Droplets with $50\,\mu$m in radius have collision efficiencies mostly above unity, primarily due to the increase of the radial relative velocity as a result of the far-field many-body interaction.

In some cases, the collision efficiency is not a monotonic function of the flow dissipation rate. For most cases, higher collision efficiency corresponds to higher flow dissipation rate, as the effects of turbulent flow increase with the flow dissipation rate. However, for the lower flow Reynolds number case and $a_2/a_1 < 0.5$, the efficiency for lower flow dissipation is slightly higher than that for higher flow dissipation. Given the larger statistic uncertainties in the data, it is not clear whether this reverse trend is due to effects of flow parameters other than the flow dissipation rate or the variation in droplet number concentration for different runs. At this stage, this non-monotonic dependence would be attributed to statistical uncertainties. Further HDNS runs with reduced statistical uncertainties are needed to fully resolve this apparent non-monotonic dependence.

All data from HDNS simulations related to the self-collisions are organized in four tables shown in appendix A. These include turbulent dynamic collision kernel, corrected radial relative velocity, corrected radial distribution function and the resulting turbulent collision efficiency. These are compiled for the purpose of guiding theoretical parameterization in the future.

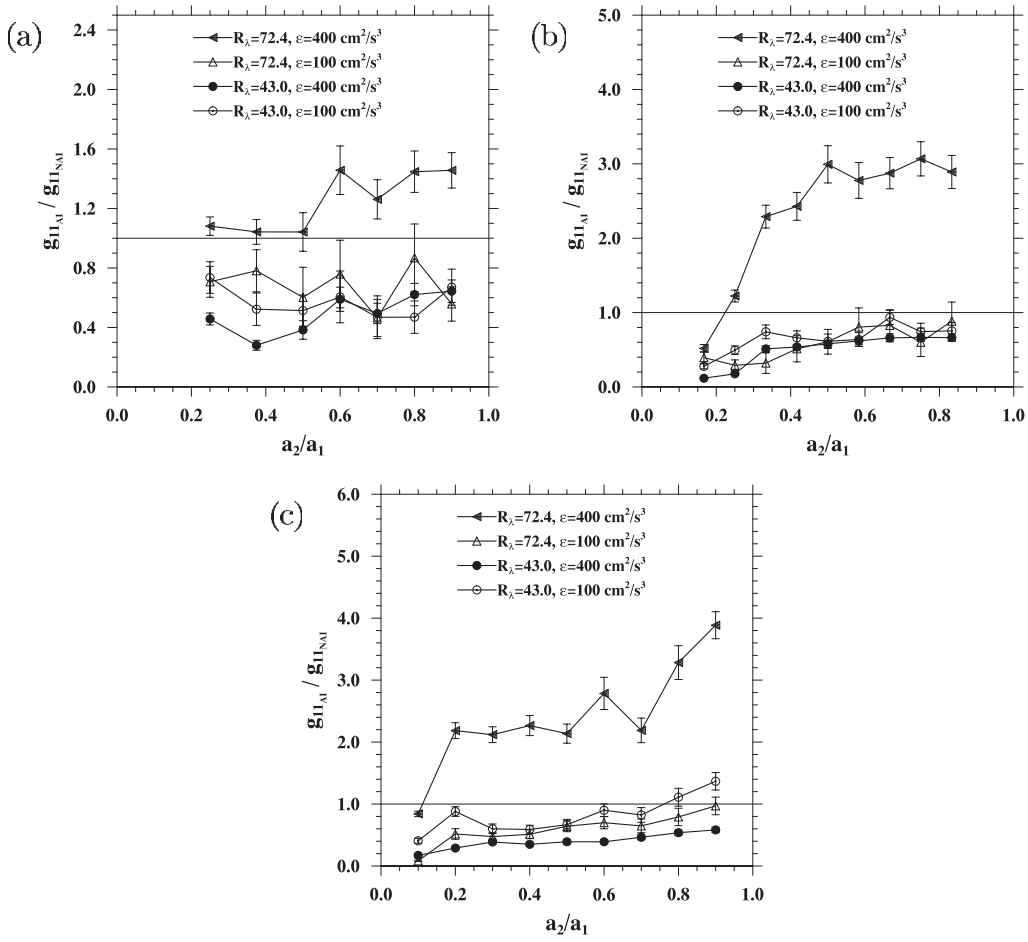

Figure 7. Ratio of the radial distribution function with AI to that corresponding to the geometric collision case for a_1–a_1 self-collisions. (a) $a_1 = 20\,\mu$m, (b) $a_1 = 30\,\mu$m and (c) $a_1 = 50\,\mu$m.

6. Results for cross-size collisions

6.1. Collision efficiency

In figure 9, we show the results of collision efficiency E_{12}^{D} based on dynamic kernels for cross-size collisions. Also shown are the results of gravitational collision efficiency E_{12}^{g} for comparison. The LWC used here are shown in table 2. They are larger than the typical value in clouds (0.5–1 g m^{-3}, [23, 24]). Therefore, the effect of the far-field AI may be overestimated in our HDNS due to both the use of Stokes disturbance flows and the higher LWC.

We find that air turbulence enhances the cross-size collision efficiency mostly because the AIs become less effective in reducing the relative motion among droplets (see section 6.2). There appears to be very little R_λ dependence of the collision efficiency as the droplets are much smaller than the Kolmogorov eddy and their disturbance flows are highly localized and mostly contained within the Kolmogorov eddy. The collision efficiency increases with the flow dissipation rate as a stronger relative motion due to the background air turbulence will undermine AI effects. Also shown in figure 9(a) are collision efficiency data from table A.2

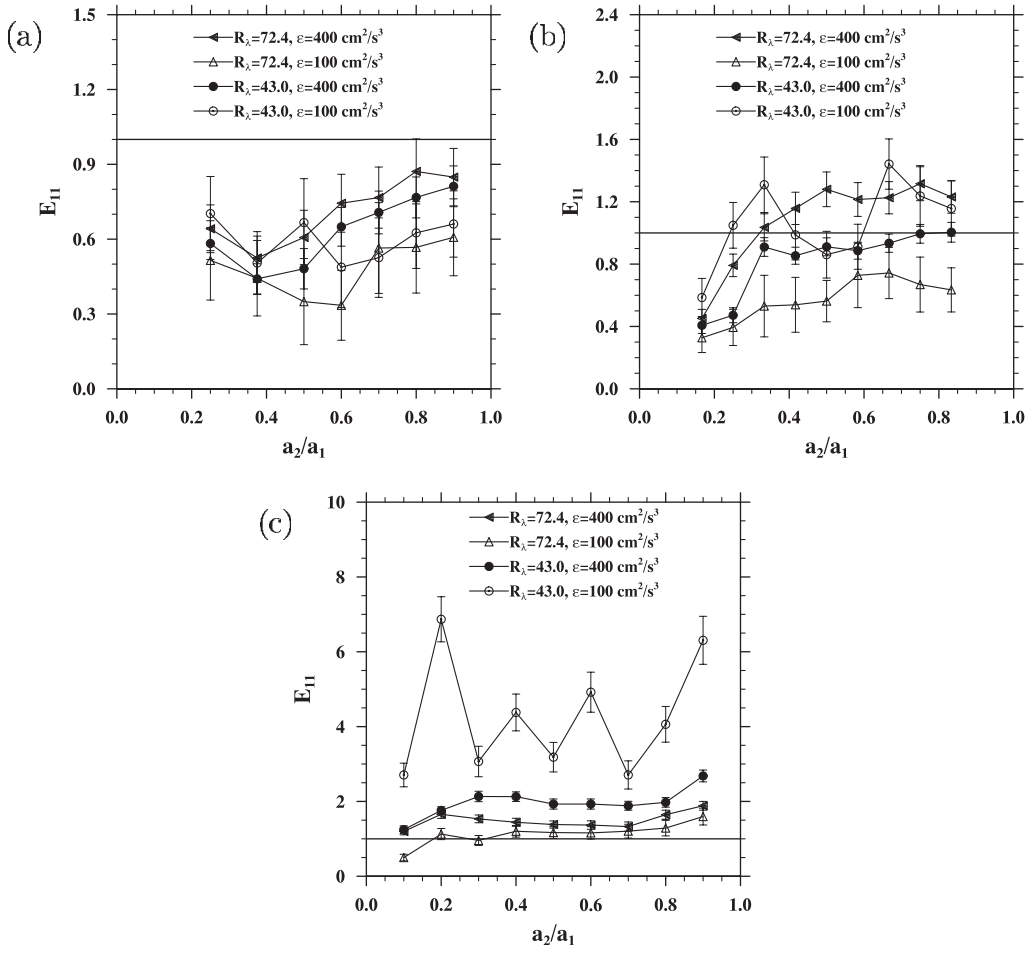

Figure 8. Turbulent collision efficiencies for a_1–a_1 self-collisions. a_2 is the radius of the other droplets simultaneously present in the flow. (a) $a_1 = 20\,\mu$m, (b) $a_1 = 30\,\mu$m and (c) $a_1 = 50\,\mu$m.

in Pinsky *et al* [25] for $a_1 = 20\,\mu$m, $\epsilon = 200\,\mathrm{cm^2\,s^{-3}}$ and $R_\lambda = 20\,000$. Similar to our data at $\epsilon = 100\,\mathrm{cm^2\,s^{-3}}$, the collision efficiency from Pinsky *et al* [25] is close to the gravitational collision efficiency, except in the region $a_2/a_1 \to 1$.

6.2. Radial relative velocity

Figure 10 exhibits the relative change of the radial relative velocity for cross-size collisions due to AI. The curves in figure 10 have similar shapes as those in figure 9, implying that the collision efficiency is primarily determined by the change in the radial relative velocity. Pairs with smaller a_2/a_1 experience a larger reduction in the relative velocity, as the smaller droplet follows more closely the streamlines of the disturbance flow induced by the larger droplet.

We find that for 50 μm collecting droplets the relative change of the radial relative velocity is not significant for a_2/a_1 larger than 0.5, perhaps due to the fact that the inertial response time τ_{p2} is comparable to or larger than the AI time $\alpha R_{12}/|v_{p1} - v_{p2}|$, where α is on the order of 10 determining the AI distance.

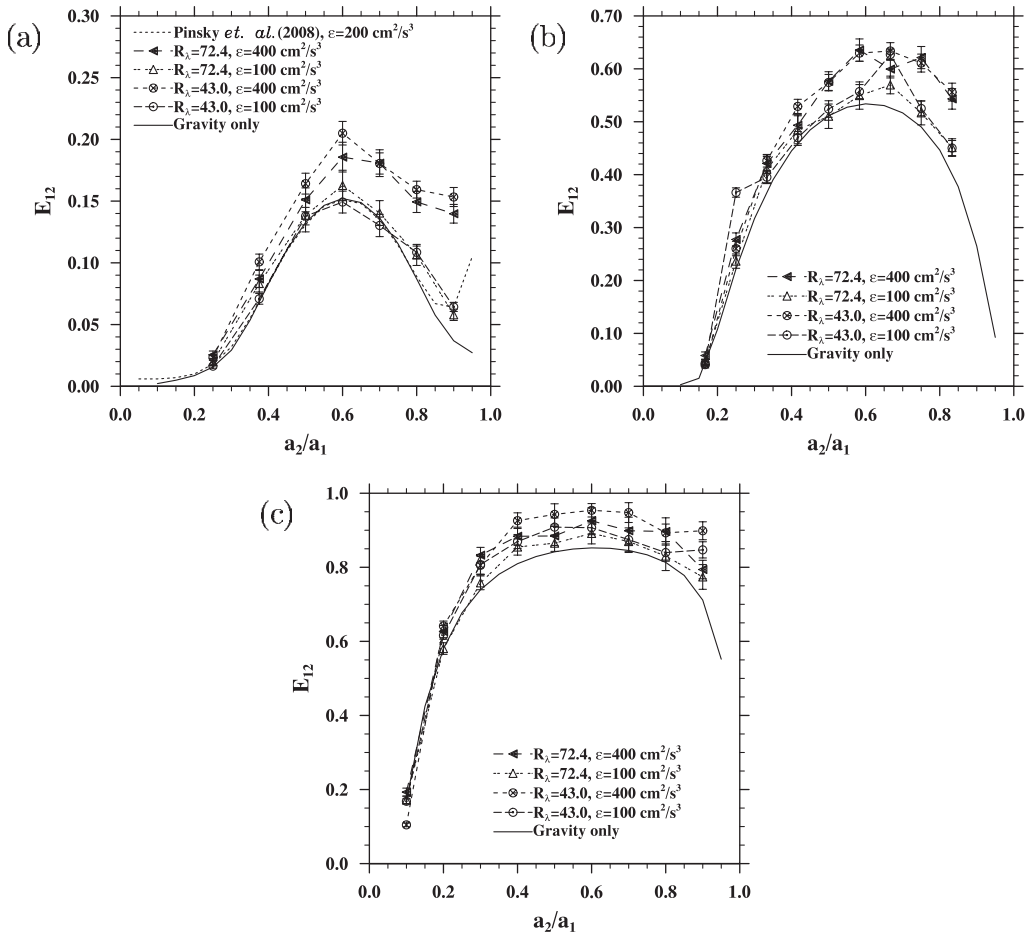

Figure 9. Turbulent collision efficiencies for cross-size collisions. (a) $a_1 = 20\,\mu$m, (b) $a_1 = 30\,\mu$m and (c) $a_1 = 50\,\mu$m.

Table 2. LWC in g m^{-3} used in some HDNS.

		$a_1 = 20\,\mu$m		$a_1 = 30\,\mu$m		$a_1 = 50\,\mu$m	
	ϵ	a_2	a_2	a_2	a_2	a_2	a_2
R_λ	(cm^2 s^{-3})	5 μm	18 μm	5 μm	25 μm	5 μm	45 μm
43.0	400	14.64	9.97	39.14	18.45	112.80	54.55
43.0	100	5.18	7.05	17.28	10.32	39.87	30.31
72.4	400	3.55	3.03	9.47	4.67	20.08	10.42
72.4	100	1.25	1.07	3.15	2.31	11.16	4.02

6.3. Radial distribution function

Figure 11 shows results of radial distribution function for cross-size collisions. Although the level of statistical uncertainties is relatively large, we can draw a few general conclusions on the effects of AI on the droplet pair clustering. Similar to results for self-collisions, the relative change in droplet clustering by AI is inversely related to the relative change in the

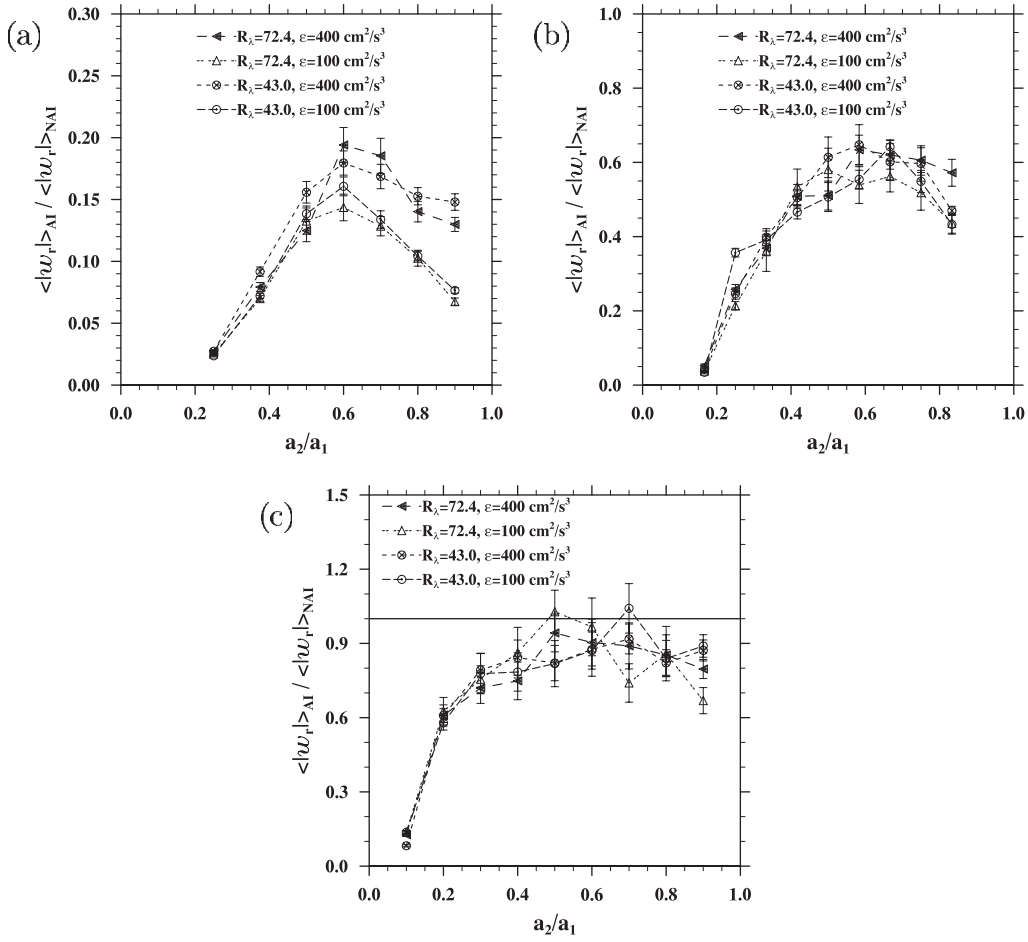

Figure 10. Ratio of the radial relative velocity with AI to that corresponding to the geometric collision case for cross-size collisions. (a) $a_1 = 20\,\mu$m, (b) $a_1 = 30\,\mu$m and (c) $a_1 = 50\,\mu$m.

radial relative velocity. The droplet clustering is significantly enhanced when a_2/a_1 is small as a result of the larger reduction in the radial relative velocity. For 20 μm collecting droplets, the relative increase in the clustering tends to level off at an almost constant value of 20% when $(a_2/a_1) \geqslant 0.5$. For larger collecting droplets, this transition occurs at smaller (a_2/a_1). For pairs with small a_2/a_1, the a_2-droplet can respond effectively to the disturbance flow induced by the a_1-droplet so that both the magnitude and the direction of the pair relative motion are modified. The pair concentration can be increased due to the increased interaction time.

Again for future reference and parameterization purposes, all data from HDNS simulations for cross-size collisions are compiled in appendix B.

6.4. Preliminary theory for $\langle|w_r|\rangle$ with AIs

As a first step toward the parametrization of the collision kernel, we shall develop a preliminary theory for the average radial relative velocity at contact for cross-size pairs with pairwise AIs. The rigorous theory for $\langle|w_r|\rangle$ developed in Ayala *et al* [16] for geometric collisions is extended here to include pairwise AI. In table 3 we compile the variances of the droplet

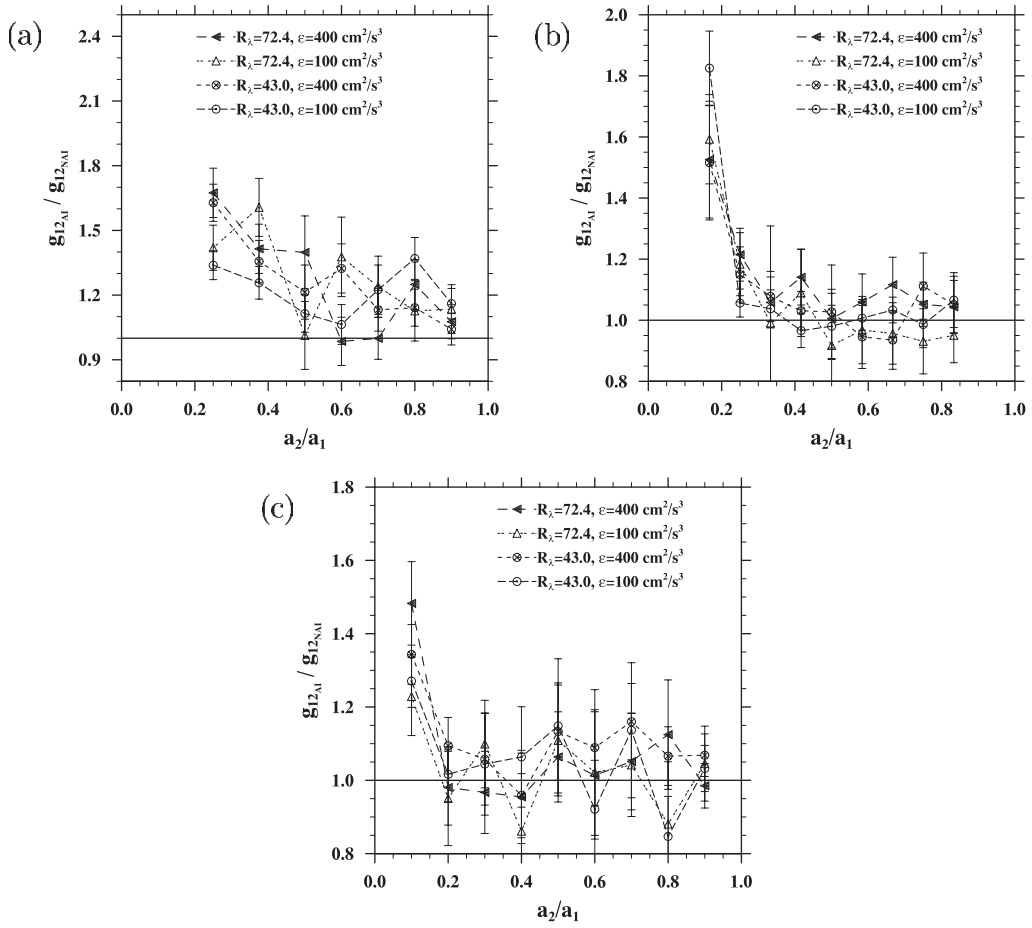

Figure 11. Ratio of the radial distribution function with AI to that corresponding to the geometric collision case for cross-size collisions. (a) $a_1 = 20\,\mu$m, (b) $a_1 = 30\,\mu$m and (c) $a_1 = 50\,\mu$m.

Table 3. Variance of the droplet velocity $\langle (v'^{(1)})^2 \rangle$ in the horizontal direction in a turbulent flow with $R_\lambda = 72.4$ and $\epsilon = 400\,\mathrm{cm^2\,s^{-3}}$.

a (μm)	NAI ($\mathrm{cm^2\,s^{-2}}$)	AI ($\mathrm{cm^2\,s^{-2}}$)	$\dfrac{\langle (v'^{(1)})^2 \rangle_{AI}}{\langle (v'^{(1)})^2 \rangle_{NAI}}$
20	155.7766	156.0867	1.0020
30	152.0732	155.1894	1.0205
50	104.4411	99.3749	0.9515

velocity in the horizontal direction in a turbulent flow with and without AIs. In addition, table 4 exhibits the velocity covariance $\langle (v'^{(1)} v'^{(2)}) \rangle$ in the horizontal direction for pairs at contact with $a_1 = 30\,\mu$m in a turbulent flow. Both tables show that AIs have little effect on the droplet velocity fluctuations in a bidisperse system. These fluctuations are governed by large-scale turbulent eddies. However, the relative motion for a colliding pair is governed by small-scale turbulent eddies and local disturbance flows. This requires consideration of pair dynamics at near-field separations.

Table 4. Droplet velocity covariance $\langle(v'^{(1)}v'^{(2)})\rangle$ in the horizontal direction for pairs at contact in a turbulent flow with $R_\lambda = 72.4$ and $\epsilon = 400\,\mathrm{cm^2\,s^{-3}}$. $a_1 = 30\,\mu\mathrm{m}$.

a_2 (μm)	NAI ($\mathrm{cm^2\,s^{-2}}$)	AI ($\mathrm{cm^2\,s^{-2}}$)	$\frac{\langle(v'^{(1)}v'^{(2)})\rangle_{\mathrm{AI}}}{\langle(v'^{(1)}v'^{(2)})\rangle_{\mathrm{NAI}}}$
5.0	151.5745	155.0389	1.0228
7.5	146.9387	143.9702	0.9797
10.0	149.7256	151.7318	1.0134
12.5	147.2431	142.7423	0.9694
15.0	158.5085	155.9374	0.9838
17.5	147.2135	153.1115	1.0401
20.0	143.4058	149.5308	1.0427
22.5	148.4993	145.6645	0.9809
25.0	148.8682	146.2661	0.9825

Here a preliminary theory is developed based on the theory of Ayala *et al* [16] for non-interacting droplets, by replacing the still-fluid terminal velocities, v_{p1} and v_{p2}, in their theory with modified settling velocities, v^*_{p1} and v^*_{p2}, of a droplet pair undergoing AI. A droplet settles faster due to the disturbance flow of the other droplet in the pair [13], and a specific analytical version of this is presented in appendix C. The predicted $\langle|w_{\mathrm{r}}|\rangle$ after this simple modification to account for AI is compared with the HDNS data in figure 12. The background turbulence corresponds to the DNS flow at $R_\lambda = 72.4$ and $\epsilon = 100\,\mathrm{cm^2\,s^{-3}}$. The theory provides a reasonable description of the effect of AI on the radial relative velocity for intermediate to large a_2/a_1 for 30 and 50 μm collecting droplets. Even for small a_2/a_1 and small collecting droplet size, the theory provides a good qualitative prediction. For example, the theory predicts a small radial relative motion for small a_2/a_1 and a maximum radial relative motion for intermediate a_2/a_1, in qualitative agreement with HDNS results.

It is important to point out that the theory addresses the near-field pairwise AI interaction only. No effort is made to model the effect of far-field many-body interaction which can account for the effect of finite particle concentrations. It is possible to include the far-field cumulative effect by following the method of Wang *et al* [13].

6.5. Turbulent enhancements

We shall now study the enhancement factors defined in section 2, namely, the enhancement factor η_{E} on the collision efficiency and the factor η_{G} on the geometric collision kernel. These factors describe the effects of turbulence when compared to the reference case of aerodynamical–gravitational coagulation.

Figures 13–15 show the enhancement factors due to turbulence for cross-size collisions. The enhancement factor η_{E} on the collision efficiency shows little dependence on R_λ and it is larger for both limiting cases $a_2/a_1 \to 1$ and $a_2/a_1 \to 0$. An enhancement up to a factor of 4 is observed for $a_2/a_1 = 0.9$ and $a_1 = 20\,\mu$m with $\epsilon = 400\,\mathrm{cm^2\,s^{-3}}$. In figure 13(a), we also compare our results with the data taken from Pinsky *et al* [25, 26] at $\epsilon = 200\,\mathrm{cm^2\,s^{-3}}$, $R_\lambda = 20\,000$ and 1000 mb pressure. Their enhancement factors were computed by combining

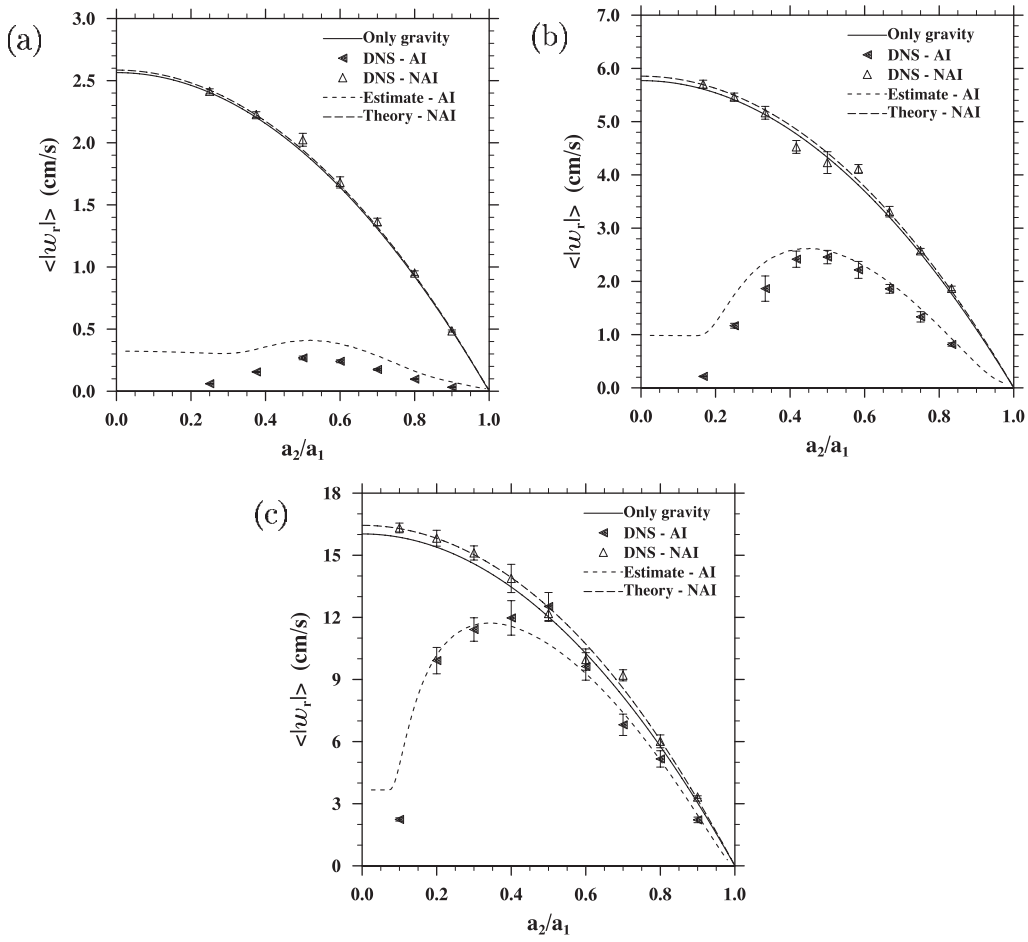

Figure 12. Comparison of theoretical estimate of the radial relative velocity with HDNS data. The turbulent flow has $R_\lambda = 72.4$ and $\epsilon = 100\,\mathrm{cm^2\,s^{-3}}$. (a) $a_1 = 20\,\mu$m, (b) $a_1 = 30\,\mu$m and (c) $a_1 = 50\,\mu$m.

the turbulent collision efficiency published in [25] and the gravitational collision efficiency published in [26]. Their results show similar trend and magnitude.

For the limit of $a_2/a_1 \to 1$, the turbulent flow produces a fluctuating far-field condition. This combined with finite droplet inertia limits the effectiveness of AIs in altering the droplet trajectories. This results in more collisions in turbulent air. For the other limit $a_2/a_1 \to 0$, the collision efficiency for the stagnant fluid case is very small. Minor modifications by turbulence such as local fluid shear and acceleration can affect the otherwise well-defined relative motion characterizing the small collision efficiency.

In general, the enhancement factor is smaller for larger a_1 as gravity plays a more dominant role in defining the disturbance flows and the time scale for AI ($\propto R/(v_{p1} - v_{p2})$) is reduced. Air turbulence is only effective in altering AI when (i) the level of turbulence fluctuations at pair separation close to contact, as governed by ϵ, is comparable to $(v_{p1} - v_{p2})$, and (ii) the AI time becomes comparable to τ_{p2}, the inertial response time of the smaller droplet.

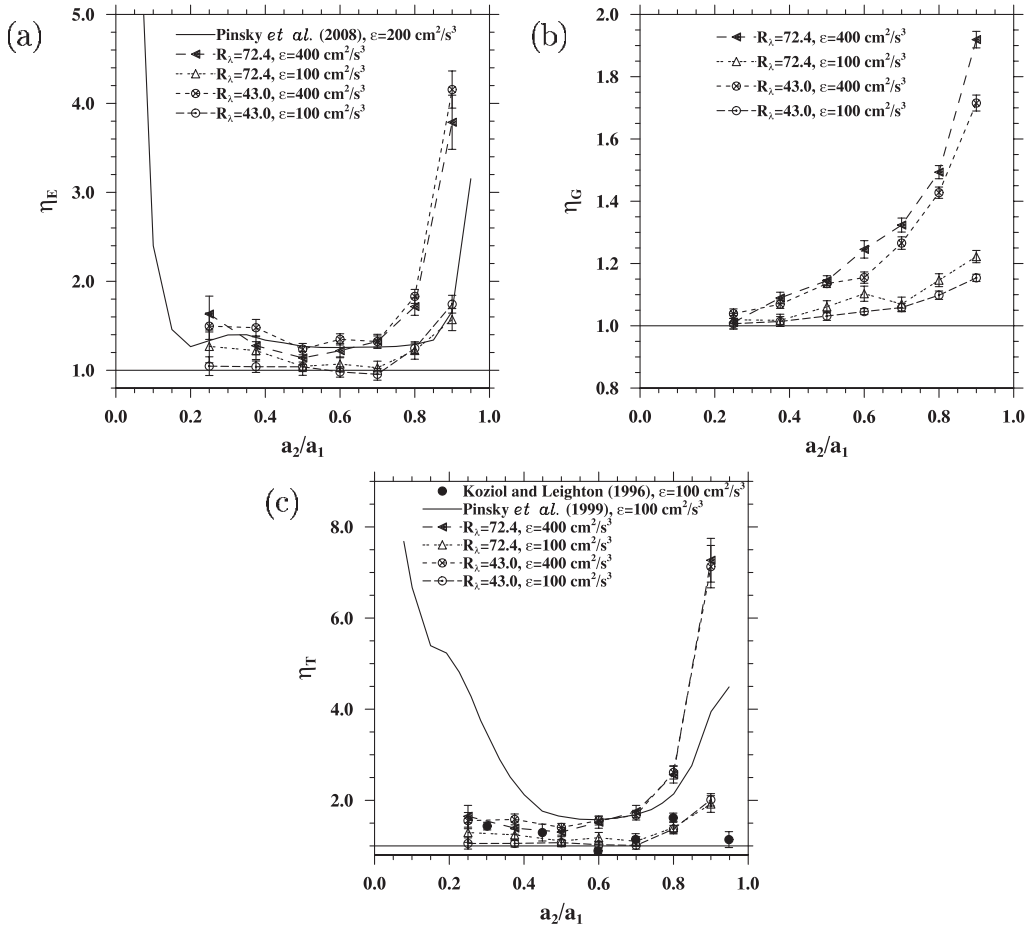

Figure 13. Turbulent enhancement factors for $a_1 = 20\,\mu$m. (a) Enhancement factor η_E on the collision efficiency, (b) enhancement factor η_G on the geometric collision kernel and (c) total enhancement factor η_T ($\eta_E\eta_G$).

The first condition may be roughly stated as

$$\frac{R(v_k/\eta)}{v_{p1} - v_{p2}} = \frac{9}{2}\frac{\rho}{\rho_w}\frac{\sqrt{\epsilon\nu}}{(a_1 - a_2)|\mathbf{g}|} \leqslant C_1, \tag{20}$$

therefore, this condition implies a larger ϵ and a value of a_2/a_1 close to one. The second condition may be stated as

$$\frac{R}{(v_{p_1} - v_{p_2})\tau_{p_2}} = \left(\frac{9}{2}\frac{\rho}{\rho_w}\right)^2 \frac{\nu^2/|\mathbf{g}|}{a_2{}^2(a_1 - a_2)} \leqslant C_2. \tag{21}$$

This condition favors the two limiting cases of $a_2/a_1 \to 0$ and $a_2/a_1 \to 1$. The above simple scaling arguments explain qualitatively the observed η_E behavior shown in figures 13(a), 14(a) and 15(a). They also explain why the effect of turbulence on η_E decreases with increasing a_1 for a fixed a_2/a_1.

The enhancement factor η_G on the geometric collision kernel depends on R_λ and ϵ as discussed in Ayala *et al* [15]. In this case, the first condition, equation (20), should be satisfied for a large η_G, namely, large ϵ and $a_2/a_1 \to 1$. This qualitatively explains the general behavior

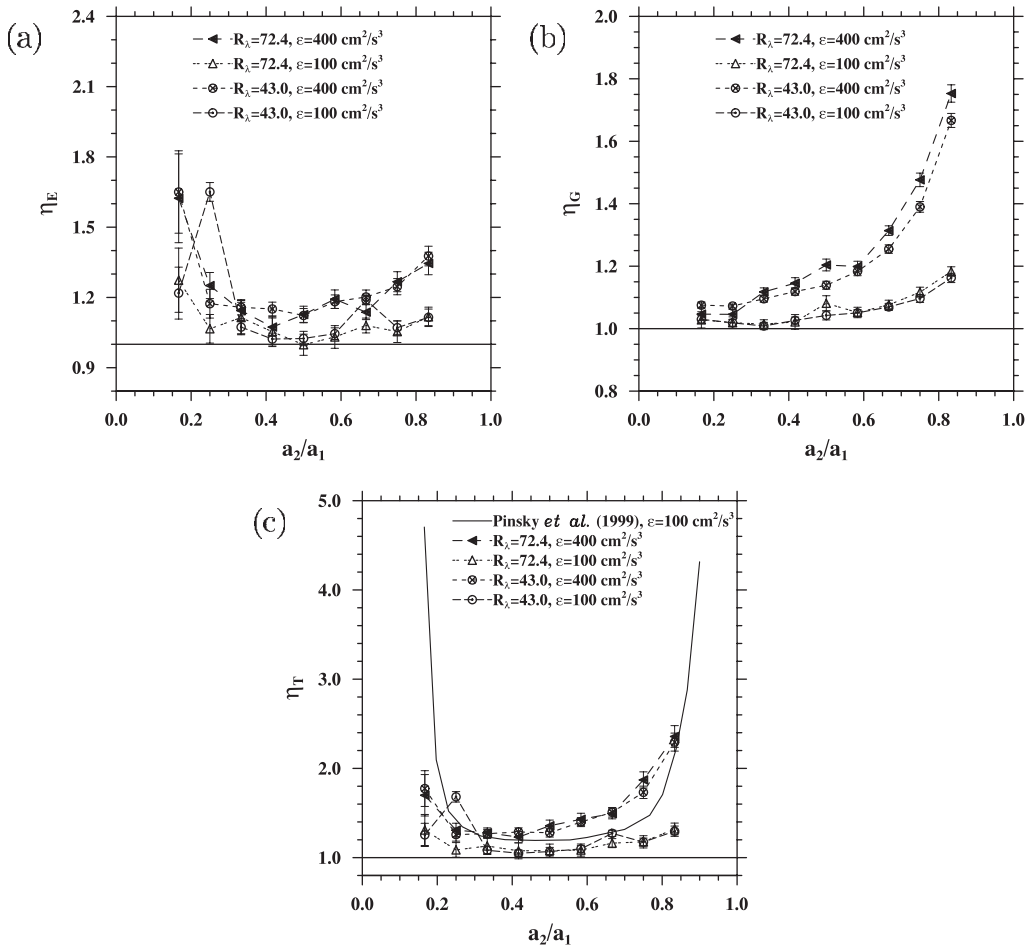

Figure 14. Turbulent enhancement factors for $a_1 = 30\,\mu$m. (a) Enhancement factor η_E on the collision efficiency, (b) enhancement factor η_G on the geometric collision kernel and (c) total enhancement factor η_T ($\eta_E\eta_G$).

in figures 13(b), 14(b) and 15(b). Other conditions for enhanced geometric collision through particle clustering would be $\tau_p \sim \tau_k$ [19] and $F_p \equiv \tau_p v_p^2/\,\Gamma_{vort} = \tau_p^3|\mathbf{g}|^2/\nu \sim 1$ [15, 27]. For $\nu = 0.17\,\mathrm{cm^2\,s^{-1}}$, $|\mathbf{g}| = 980\,\mathrm{cm\,s^{-2}}$, $\rho_w/\rho \approx 1000$, the condition $F_p \sim 1$ implies

$$a_p \sim 21\,\mu\mathrm{m}. \tag{22}$$

The condition of $\tau_p \sim \tau_k$ yields

$$a_p(\mu_m) \sim \frac{177}{[\epsilon(\mathrm{in\ cm^2\,s^{-3}})]^{0.25}}. \tag{23}$$

For the range of dissipation rate in clouds ($\epsilon \leqslant 5000\,\mathrm{cm^3\,s^{-2}}$), we then expect that the preferential concentration is important for

$$21\,\mu\mathrm{m} \leqslant a_p(\mu_m) \leqslant \frac{177}{[\epsilon(\mathrm{in\ cm^2\,s^{-3}})]^{0.25}}.$$

This range is $21\,\mu\mathrm{m} \leqslant a_p \leqslant 56\,\mu\mathrm{m}$ for $\epsilon = 100\,\mathrm{cm^3\,s^{-2}}$ and $21\,\mu m \leqslant a_p \leqslant 40\,\mu\mathrm{m}$ for $\epsilon = 400\,\mathrm{cm^3\,s^{-2}}$.

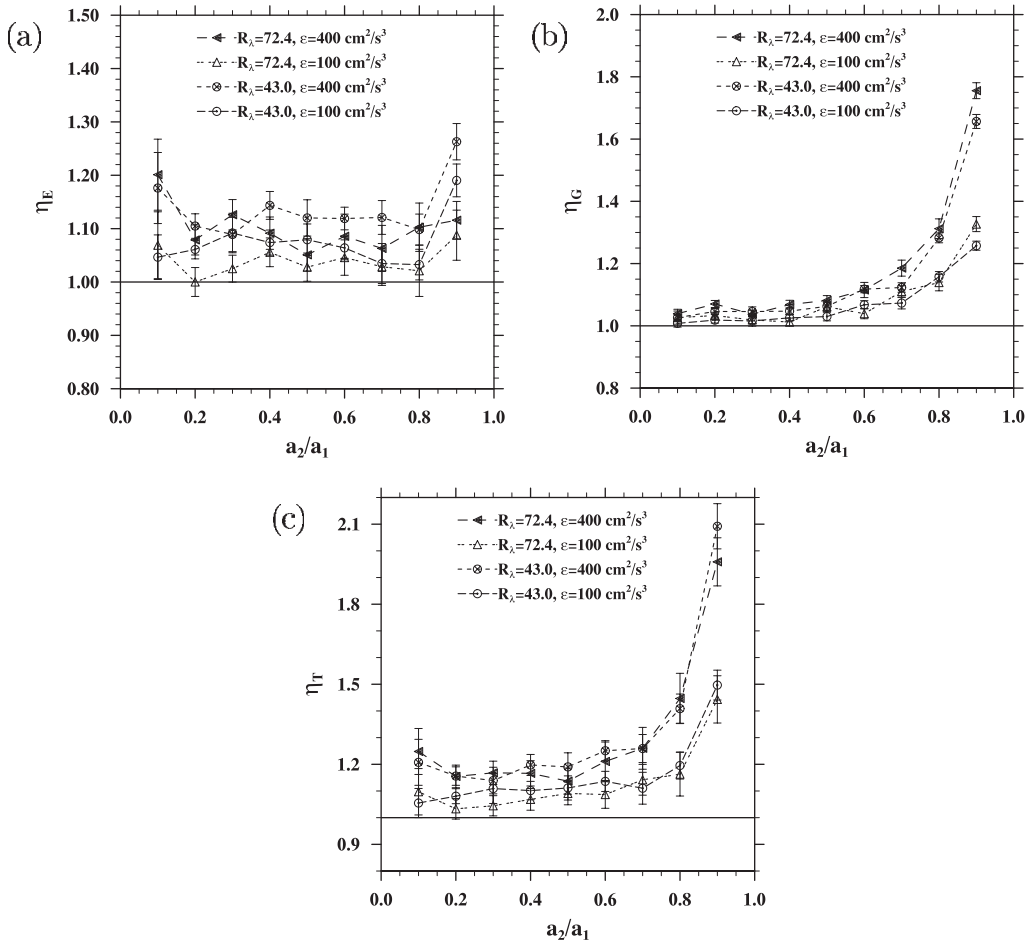

Figure 15. Turbulent enhancement factors for $a_1 = 50\,\mu$m. (a) Enhancement factor η_E on the collision efficiency, (b) enhancement factor η_G on the geometric collision kernel and (c) total enhancement factor η_T ($\eta_E\eta_G$).

The overall enhancement factor by turbulence η_T is equal to $\eta_E\eta_G$ and is shown in figures 13(c), 14(c) and 15(c). This can be in the range of 2–7 when $a_2/a_1 \sim 1$, for the two dissipation rates shown. The maximum overall enhancement of about 7 occurs for $a_1 = 20\,\mu$m, $a_2 = 18\,\mu$m and $\epsilon = 400\,\text{cm}^3\,\text{s}^{-2}$. For most intermediate size ratios, the overall enhancement is less than 2.

Finally, we compare briefly our DNS results with published results by Koziol and Leighton [10] and Pinsky *et al* [11]. We shall focus on the total enhancement factor η_T. The Koziol and Leighton's results for $\epsilon = 100\,\text{cm}^2\,\text{s}^{-3}$ are in reasonable agreement with our results, except for $a_2/a_1 = 0.95$ where they did not observed a large enhancement. Given the qualitative arguments by equations (20) and (21), we suspect that the KL result at $a_2/a_1 = 0.95$ might not be correct. The results by Pinsky *et al* [11] are a factor of 2 to 3 larger than our results for $a_2/a_1 \sim 1$ and a factor of 1.3–4 larger than ours at $a_2/a_1 \approx 0.25$. Part of the reason for this discrepancy is probably due to the approximate representation of the air flow used by Pinsky *et al* [11]. The results of Pinsky *et al* [11] agree qualitatively with the present results in that the overall enhancement factor peaks at both $a_2/a_1 \to 1$ and $a_2/a_1 \to 0$, consistent with the arguments given by equations (20) and (21).

7. Summary and concluding remarks

In this paper, we computed the collision efficiency of sedimenting cloud droplets in turbulent air using a HDNS approach [6]. The HDNS approach considered simultaneously the effects of air turbulence, droplet–droplet AI, droplet inertia and gravitational sedimentation. The air turbulence within clouds was assumed to be homogeneous and isotropic, and its small-scale motion (1 mm–10 cm scales) was computationally generated by direct numerical integration of the full Navier–Stokes equations. Local, small-scale (10 μm–1 mm) disturbance flows induced by the presence of droplets were represented analytically by an improved superposition method [6, 28]. The HDNS approach coupled the disturbance flows with the background air turbulence, and is capable of representing both the strong near-field droplet–droplet AI and the far-field weak but cumulative AI [13]. When the disturbance flows are switched off, HDNS reduces to the usual point-particle based DNS that has been used by many to study the geometric collision kernel of sedimenting droplets [15].

The interpretation of the HDNS results was based on the theoretical formulation developed by Wang *et al* [5]. They showed that a kinematic formulation similar to that for the geometric collision kernel exists for aerodynamically interacting droplets, after near-field corrections due to the non-overlap requirement are included. The turbulent collision efficiency η_{E} can then be computed either in terms of dynamical collision events or in terms of kinematic pair statistics (the radial relative velocity and radial distribution function). Comparisons of these statistics with their respective values for geometric collision also provided insight into the exact nature how the AI alters the collision process of sedimenting finite-inertia droplets.

We found that air turbulence enhances the collision efficiency partly due to the fact that AIs become less effective in reducing the relative motion of droplets in the presence of background air turbulence. The level of increase in the collision efficiency for cross-size collisions depends primarily on the flow dissipation rate and the size ratio a_2/a_1. For instance, the collision efficiency between droplets of 18 and 20 μm in radii is increased, relative to the gravitational collision efficiency in stagnant air, by a factor of 4 and 1.6 by air turbulence at dissipation rates of 400 and 100 $\mathrm{cm}^2\,\mathrm{s}^{-3}$, respectively. Qualitative explanations for the observed variations in η_{E} were provided. For most cross-size collisions, we observed that AIs reduce the average radial relative velocity but also increase the radial distribution function. The collision efficiency for self-collisions in a bidisperse turbulent suspension can be larger than one. Such an increase in self-collisions is related to the far-field many-body AI and depends on the volumetric concentration of droplets of all sizes in the system. The level of LWCs used in this paper is somewhat larger than that in real clouds, the practical relevance of this new observation to clouds remains to be resolved in future HDNS simulations using more realistic LWC. A preliminary theory for the radial relative velocity was developed and was shown to provide a good description of the effect of AI on the radial relative motion for large collecting droplets and intermediate to large size ratio a_2/a_1.

The enhancement factors by turbulence on the collision efficiency and the geometric collision kernel were calculated separately. The total enhancement factors agreed qualitatively with previous results of Koziol and Leighton [10] and Pinsky *et al* [11] and quantitatively with the more recent results of Pinsky *et al* [25]. In the case of cross-size collisions between droplets of 18 and 20 μm in radii, air turbulence resulted in a total enhancement, relative to the stagnant air case, by a factor of 7 and 2 at dissipation rates of 400 and 100 $\mathrm{cm}^2\,\mathrm{s}^{-3}$, respectively. For intermediate size ratios ($0.2 < a_2/a_1 < 0.8$), the overall enhancement typically falls below 2.

Scaling arguments show that the overall enhancement factor tends to peak at the two limiting cases of $a_2/a_1 \to 1$ and $a_2/a_1 \to 0$.

The results obtained in this work imply that the small-scale turbulent air motion in the atmosphere could play an important role in the initiation and development of rain droplets from cloud droplets, which may help better explain the rapid onset of rain in cumulus clouds, as shown in [29].

It should be noted that HDNS simulations are much more expensive to perform computationally [6], than the geometric collision of point or ghost particles. For this reason, not all ranges of size combination and dissipation rate relative to cloud droplets have been considered in this paper. It is also desirable to re-run some of the cases over a longer time interval to reduce the statistical uncertainty. When the size ratio a_2/a_1 is very small, a very small time step must be used to solve the droplet equation of motion. In this case, asymptotic expansions for the droplet velocity such as those proposed in [30] could be used to eliminate the need for numerical integration. The full potential of HDNS will continue to be explored as we conduct more simulations over a wider parameter range including higher flow Reynolds numbers. Our ultimate goal is to develop a theoretical parametrization for the turbulent collision efficiency, based on improved understanding and rich data from HDNS.

While the HDNS approach currently represents the best available method for treating turbulent collision of sedimenting cloud droplets, there are areas where the approach should be developed further. One area is a more efficient implementation of the HDNS approach. The most time consuming part of HDNS is the computation of the disturbance flow velocities. Other numerical methods to solve very large sparse linear systems of equations for the disturbance flow velocities should be explored. Another area is improved accuracy for the short-range AI force such as the lubrication force. Some preliminary work in this direction has been reported in [31].

Our results here demonstrate that two interaction mechanisms could operate in real clouds: the short-range droplet-pair binary interaction and the long-range many-body interaction. The open question is the relative importance of the two interaction mechanisms for the case of cloud droplets. With increasing computing resources, we expect to apply the HDNS to more realistic LWCs so the relative importance of long-range many-body interaction can be quantified.

Finally, the relative motion of large cloud droplets ($50\,\mu$m or larger) is affected by a range of turbulent eddies including inertial-range eddies which may not be fully represented in the simulations [32]. The dissipation-range structure and statistics (intermittency and acceleration) of the air turbulence depend on the flow Reynolds number. It is hoped that the improved understanding of turbulent hydrodynamic interaction reported here will motivate better theoretical treatment of collision efficiency that could bypass the limitations of the HDNS.

Acknowledgments

This study has been supported by the National Science Foundation through grants ATM-0114100 and ATM-0527140, and by the National Center for Atmospheric Research (NCAR). NCAR is sponsored by the National Science Foundation. LPW also acknowledges support from National Natural Science Foundation of China (project no 10628206). Most of the simulations were conducted using the SGI Origin 3800/2100 and IBM clusters at NCAR. OA is grateful for the additional computing resources provided by the Scientific Computing Division at NCAR.

Appendix A. HDNS statistics for self-collisions

All data from HDNS simulations related to the self-collisions are organized in four tables in terms of turbulent dynamic collision kernel (table A.1), corrected radial relative velocity (table A.2), corrected radial distribution function (table A.3), and the resulting turbulent collision efficiency (table A.4). These are compiled for the purpose of guiding theoretical parameterization in the future. They could also be compared with tables in Ayala *et al* [15] for geometric collisions. Since the self-collision statistics are affected by the presence of the second-size droplets, the tables also show a_2/a_1 as a parameter. Table A.4 clearly shows that the collision efficiency for self-collision can be larger than one if another group of droplets of similar size are present.

We wish to point out that the results for the 50 μm droplets should be used with caution. In reality, such large droplets have a particle Reynolds number on the order of or larger than one, so that the disturbance flow does not follow the Stokes flow theory. The Stokes disturbance flows used here tend to overestimate the collision efficiency.

Appendix B. HDNS statistics for cross-size collisions

All data from HDNS simulations for cross-size collisions are compiled here, including turbulent dynamic collision kernel (table B.1), corrected radial relative velocity (table B.2), corrected radial distribution function (table B.3) and the resulting enhancement factor of collision efficiency by turbulence (table B.4). The enhancement factor in table B.4 is computed by dividing the turbulent collision efficiency by the gravitational collision efficiency computed using the improved superposition method as described in [28].

Appendix C. Radial relative velocity for a pair of aerodynamically-interacting droplets

Integrating equation (15), the particle velocity including the disturbance flow can be formally written as [33]

$$V_i^{(k)} = \int_{-\infty}^{t} \frac{U_i(\mathbf{Y}^{(k)}(\tau), \tau)}{\tau_{p_k}} \exp\left(\frac{\tau - t}{\tau_{p_k}}\right) \mathrm{d}\tau + \int_{-\infty}^{t} \frac{u_i^{(k)}}{\tau_{p_k}} \exp\left(\frac{\tau - t}{\tau_{p_k}}\right) \mathrm{d}\tau + v_{p_k}\delta_{i3}. \tag{C.1}$$

On the rhs of the equation, the first term is due to the background air turbulence and has been treated in Ayala *et al* [16]. The second term on the rhs is due to the AI. The last term is the terminal velocity. As a preliminary theory, we decouple the AI term from the first term and model the AI term together with the gravity term. Namely, a modified terminal velocity is introduced as

$$\mathbf{V}_p^{(k)} = \int_{-\infty}^{t} \frac{\mathbf{u}^{(k)}}{\tau_{p_k}} \exp\left(\frac{\tau - t}{\tau_{p_k}}\right) \mathrm{d}\tau + v_{p_k}\mathbf{k}. \tag{C.2}$$

The next approximation is to treat the AI term in the vertical direction only by assuming that the a_1-droplet is capturing the a_2-droplet along a single vertical line. Thus, setting the reference time for the capture to $t = 0$, an estimate of the modified terminal velocity can be written as

$$v_{p_k}^* \approx \int_{-\infty}^{0} \frac{u_3^{(k)}}{\tau_{p_k}} \exp\left(\frac{\tau}{\tau_{p_k}}\right) \mathrm{d}\tau + v_{p_k}. \tag{C.3}$$

Table A.1. HDNS results of Γ (in $\mathrm{cm^3\,s^{-1}}$) of self-collisions in the presence of a_2-droplets for different Taylor microscale Reynolds number R_λ, and turbulent dissipation rate ϵ. The values between parentheses are the corresponding statistical uncertainties ($\pm$ one standard deviation).

		R_λ			
		43.0		72.4	
a_1	a_2/a_1	ϵ ($\mathrm{cm^2\,s^{-3}}$)		ϵ ($\mathrm{cm^2\,s^{-3}}$)	
(μm)		100.0	400.0	100.0	400.00
20.0	0.250	3.30E-06 (2.67E-07)	1.29E-05 (6.52E-07)	2.65E-06 (3.86E-07)	1.25E-05 (8.13E-07)
20.0	0.375	2.37E-06 (2.81E-07)	9.77E-06 (7.56E-07)	2.29E-06 (4.06E-07)	1.02E-05 (8.43E-07)
20.0	0.500	3.13E-06 (4.16E-07)	1.07E-05 (1.15E-06)	1.80E-06 (5.95E-07)	1.18E-05 (1.13E-06)
20.0	0.600	2.29E-06 (4.58E-07)	1.44E-05 (8.56E-07)	1.73E-06 (4.39E-07)	1.45E-05 (1.04E-06)
20.0	0.700	2.47E-06 (4.25E-07)	1.57E-05 (9.56E-07)	2.91E-06 (4.62E-07)	1.49E-05 (1.13E-06)
20.0	0.800	2.93E-06 (2.86E-07)	1.70E-05 (7.96E-07)	2.92E-06 (4.66E-07)	1.70E-05 (1.11E-06)
20.0	0.900	3.10E-06 (2.18E-07)	1.80E-05 (7.31E-07)	3.13E-06 (2.82E-07)	1.65E-05 (8.50E-07)
30.0	0.167	1.50E-05 (1.81E-06)	1.11E-04 (1.07E-05)	9.89E-06 (1.63E-06)	8.33E-05 (6.63E-06)
30.0	0.250	2.68E-05 (1.38E-06)	1.28E-04 (9.07E-06)	1.19E-05 (2.03E-06)	1.46E-04 (6.04E-06)
30.0	0.333	3.35E-05 (1.59E-06)	2.47E-04 (8.61E-06)	1.60E-05 (3.98E-06)	1.91E-04 (6.52E-06)
30.0	0.417	2.53E-05 (1.88E-06)	2.32E-04 (7.62E-06)	1.63E-05 (3.30E-06)	2.14E-04 (8.43E-06)
30.0	0.500	2.20E-05 (1.89E-06)	2.47E-04 (7.92E-06)	1.70E-05 (1.90E-06)	2.36E-04 (8.71E-06)
30.0	0.583	2.33E-05 (1.64E-06)	2.41E-04 (7.22E-06)	2.20E-05 (3.53E-06)	2.24E-04 (8.79E-06)
30.0	0.667	3.69E-05 (8.71E-07)	2.54E-04 (8.03E-06)	2.25E-05 (2.18E-06)	2.26E-04 (7.77E-06)
30.0	0.750	3.17E-05 (2.18E-06)	2.70E-04 (7.92E-06)	2.02E-05 (2.82E-06)	2.43E-04 (7.93E-06)
30.0	0.833	2.96E-05 (1.91E-06)	2.73E-04 (8.75E-06)	1.92E-05 (1.89E-06)	2.27E-04 (7.94E-06)
50.0	0.100	5.58E-04 (2.48E-05)	1.19E-03 (5.41E-05)	1.63E-04 (1.77E-05)	1.20E-03 (4.86E-05)
50.0	0.200	1.42E-03 (2.16E-05)	1.67E-03 (3.06E-05)	3.68E-04 (2.31E-05)	1.66E-03 (5.08E-05)
50.0	0.300	6.32E-04 (3.80E-05)	2.03E-03 (5.86E-05)	3.12E-04 (2.17E-05)	1.53E-03 (4.91E-05)
50.0	0.400	9.02E-04 (3.60E-05)	2.02E-03 (4.77E-05)	3.92E-04 (2.37E-05)	1.44E-03 (5.59E-05)
50.0	0.500	6.56E-04 (3.38E-05)	1.84E-03 (6.18E-05)	3.81E-04 (2.50E-05)	1.38E-03 (4.71E-05)
50.0	0.600	1.01E-03 (3.69E-05)	1.84E-03 (6.18E-05)	3.78E-04 (2.80E-05)	1.37E-03 (6.51E-05)
50.0	0.700	5.58E-04 (3.71E-05)	1.79E-03 (4.82E-05)	3.94E-04 (3.31E-05)	1.33E-03 (7.62E-05)
50.0	0.800	8.37E-04 (3.77E-05)	1.88E-03 (5.38E-05)	4.20E-04 (3.90E-05)	1.65E-03 (6.28E-05)
50.0	0.900	1.30E-03 (3.80E-05)	2.55E-03 (5.72E-05)	5.21E-04 (3.74E-05)	1.88E-03 (5.09E-05)

Table A.2. HDNS results of $\langle |w_r| \rangle$ (in cm s^{-1}) of self-collisions in the presence of a_2-droplets for different Taylor microscale Reynolds number R_λ, and turbulent dissipation rate ϵ. The values between parentheses are the corresponding statistical uncertainties (± one standard deviation).

		R_λ			
		43.0		72.4	
a_1	a_2/a_1	ϵ (cm^2 s^{-3})		ϵ (cm^2 s^{-3})	
(μm)		100.0	400.0	100.0	400.00
20.0	0.250	0.02428 (0.00019)	0.05794 (0.00046)	0.02241 (0.00031)	0.05357 (0.00068)
20.0	0.375	0.02438 (0.00073)	0.06979 (0.00123)	0.01785 (0.00036)	0.04753 (0.00118)
20.0	0.500	0.02983 (0.00080)	0.05734 (0.00189)	0.01988 (0.00116)	0.05514 (0.00146)
20.0	0.600	0.02130 (0.00088)	0.05082 (0.00129)	0.01482 (0.00107)	0.04833 (0.00171)
20.0	0.700	0.02837 (0.00133)	0.06483 (0.00146)	0.03324 (0.00119)	0.05520 (0.00166)
20.0	0.800	0.03281 (0.00099)	0.06028 (0.00171)	0.01978 (0.00087)	0.05358 (0.00164)
20.0	0.900	0.02753 (0.00068)	0.06062 (0.00135)	0.03186 (0.00094)	0.05305 (0.00121)
30.0	0.167	0.06351 (0.00120)	0.30489 (0.01719)	0.03918 (0.00061)	0.32329 (0.02095)
30.0	0.250	0.06600 (0.00109)	0.24300 (0.01645)	0.05230 (0.00255)	0.17073 (0.00713)
30.0	0.333	0.05404 (0.00088)	0.16979 (0.00614)	0.08067 (0.02028)	0.12355 (0.00429)
30.0	0.417	0.04689 (0.00136)	0.14917 (0.00417)	0.04157 (0.00221)	0.12939 (0.00735)
30.0	0.500	0.05121 (0.00505)	0.13574 (0.00658)	0.04395 (0.00257)	0.11305 (0.00481)
30.0	0.583	0.04606 (0.00155)	0.13565 (0.01104)	0.04029 (0.00235)	0.12204 (0.00829)
30.0	0.667	0.05061 (0.00084)	0.11632 (0.00553)	0.04344 (0.00353)	0.10557 (0.00401)
30.0	0.750	0.05620 (0.00355)	0.14306 (0.00904)	0.04895 (0.00276)	0.12056 (0.00636)
30.0	0.833	0.05378 (0.00198)	0.12968 (0.00642)	0.03516 (0.00262)	0.11410 (0.00656)
50.0	0.100	0.27759 (0.00536)	0.89065 (0.02162)	0.27708 (0.01445)	0.58979 (0.01787)
50.0	0.200	0.32395 (0.00836)	0.74718 (0.01510)	0.10690 (0.00795)	0.38696 (0.01378)
50.0	0.300	0.21256 (0.01813)	0.77437 (0.04770)	0.09816 (0.00536)	0.39204 (0.02353)
50.0	0.400	0.27002 (0.01772)	0.80385 (0.05828)	0.11070 (0.00730)	0.29855 (0.01808)
50.0	0.500	0.21199 (0.02223)	0.52111 (0.03299)	0.09643 (0.00754)	0.35077 (0.02661)
50.0	0.600	0.24484 (0.01667)	0.52111 (0.03299)	0.09610 (0.01040)	0.26240 (0.02272)
50.0	0.700	0.16090 (0.02495)	0.53270 (0.03616)	0.10312 (0.01314)	0.31930 (0.02844)
50.0	0.800	0.15987 (0.01261)	0.50565 (0.02868)	0.07810 (0.00567)	0.27265 (0.01853)
50.0	0.900	0.19300 (0.00940)	0.60438 (0.02563)	0.08449 (0.00552)	0.25852 (0.01225)

Table A.3. HDNS results of g_{11} of self-collisions in the presence of a_2-droplets for different Taylor microscale Reynolds number R_λ, and turbulent dissipation rate ϵ. The values between parentheses are the corresponding statistical uncertainties ($\pm$ one standard deviation).

		R_λ			
		43.0		72.4	
a_1	a_2/a_1	ϵ (cm^2 s^{-3})		ϵ (cm^2 s^{-3})	
(μm)		100.0	400.0	100.0	400.00
20.0	0.250	1.4244 (0.0356)	2.2991 (0.0530)	1.2825 (0.0520)	2.3394 (0.0724)
20.0	0.375	1.0119 (0.0905)	1.4085 (0.0769)	1.4175 (0.1061)	2.2563 (0.1199)
20.0	0.500	0.9946 (0.0831)	1.9287 (0.1885)	1.0925 (0.2516)	2.2549 (0.2206)
20.0	0.600	1.1721 (0.1970)	2.9658 (0.2188)	1.3777 (0.2659)	3.1533 (0.2693)
20.0	0.700	0.9075 (0.1700)	2.4860 (0.1842)	0.8414 (0.1372)	2.7298 (0.2125)
20.0	0.800	0.9083 (0.1025)	3.1254 (0.1769)	1.5753 (0.2451)	3.1318 (0.2180)
20.0	0.900	1.2989 (0.0800)	3.2395 (0.1725)	1.0124 (0.1017)	3.1517 (0.1742)
30.0	0.167	1.0672 (0.0491)	1.5554 (0.1137)	1.2743 (0.0618)	1.6311 (0.1224)
30.0	0.250	1.9055 (0.0737)	2.3408 (0.1229)	0.9418 (0.0882)	3.8511 (0.1535)
30.0	0.333	2.8579 (0.1377)	6.7868 (0.3161)	1.0351 (0.2871)	7.2115 (0.2991)
30.0	0.417	2.5432 (0.1696)	7.1220 (0.2574)	1.6549 (0.3146)	7.6468 (0.3944)
30.0	0.500	2.3664 (0.1931)	7.6830 (0.3845)	1.9615 (0.2373)	9.4250 (0.5471)
30.0	0.583	2.4564 (0.1722)	8.2070 (0.4339)	2.5987 (0.4335)	8.7442 (0.5336)
30.0	0.667	3.6041 (0.0940)	8.7530 (0.4494)	2.6719 (0.2727)	9.0530 (0.4294)
30.0	0.750	2.8652 (0.2191)	8.8413 (0.4544)	1.9393 (0.3220)	9.6589 (0.4775)
30.0	0.833	2.9066 (0.2087)	8.7916 (0.4087)	2.8572 (0.3896)	9.1034 (0.4657)
50.0	0.100	3.2596 (0.1017)	2.0991 (0.0642)	0.9062 (0.0618)	2.6654 (0.0928)
50.0	0.200	7.0401 (0.1620)	3.5334 (0.1176)	5.5762 (0.5343)	6.9203 (0.2870)
50.0	0.300	4.8053 (0.3107)	4.7231 (0.1808)	5.1255 (0.3096)	6.7148 (0.2902)
50.0	0.400	4.7222 (0.2400)	4.2684 (0.1784)	5.5172 (0.3664)	7.1809 (0.3900)
50.0	0.500	5.3375 (0.3418)	4.7655 (0.2125)	6.9240 (0.4601)	6.7688 (0.3738)
50.0	0.600	7.2077 (0.3400)	4.7655 (0.2125)	7.5366 (0.5258)	8.8241 (0.6735)
50.0	0.700	6.5968 (0.5172)	5.6539 (0.2631)	6.9832 (0.7025)	6.9353 (0.5100)
50.0	0.800	8.8876 (0.5699)	6.5468 (0.2571)	8.5383 (0.9098)	10.3995 (0.6859)
50.0	0.900	10.9466 (0.4114)	7.0945 (0.2375)	10.4568 (0.7951)	12.3115 (0.4816)

Table A.4. HDNS results of E_{11} of self-collisions in the presence of a_2-droplets for different Taylor microscale Reynolds number R_λ, and turbulent dissipation rate ϵ. The values between parentheses are the corresponding statistical uncertainties ($\pm$ one standard deviation).

		R_λ			
		43.0		72.4	
a_1	a_2/a_1	ϵ (cm^2 s^{-3})		ϵ (cm^2 s^{-3})	
(μm)		100.0	400.0	100.0	400.00
20.0	0.250	0.7027 (0.1487)	0.5827 (0.0645)	0.5150 (0.1591)	0.6417 (0.0958)
20.0	0.375	0.5044 (0.1260)	0.4409 (0.0606)	0.4435 (0.1513)	0.5249 (0.0875)
20.0	0.500	0.6666 (0.1759)	0.4814 (0.0809)	0.3497 (0.1726)	0.6068 (0.1091)
20.0	0.600	0.4879 (0.1615)	0.6496 (0.0777)	0.3349 (0.1401)	0.7441 (0.1161)
20.0	0.700	0.5260 (0.1594)	0.7072 (0.0857)	0.5645 (0.1820)	0.7667 (0.1226)
20.0	0.800	0.6254 (0.1428)	0.7674 (0.0820)	0.5672 (0.1832)	0.8716 (0.1303)
20.0	0.900	0.6608 (0.1329)	0.8120 (0.0818)	0.6075 (0.1541)	0.8488 (0.1151)
30.0	0.167	0.5857 (0.1226)	0.4074 (0.0521)	0.3274 (0.0945)	0.4513 (0.0585)
30.0	0.250	1.0488 (0.1467)	0.4721 (0.0481)	0.3939 (0.1161)	0.7920 (0.0723)
30.0	0.333	1.3091 (0.1777)	0.9097 (0.0600)	0.5309 (0.1975)	1.0358 (0.0871)
30.0	0.417	0.9875 (0.1608)	0.8537 (0.0546)	0.5390 (0.1761)	1.1577 (0.1036)
30.0	0.500	0.8606 (0.1497)	0.9111 (0.0575)	0.5628 (0.1328)	1.2800 (0.1112)
30.0	0.583	0.9114 (0.1444)	0.8859 (0.0541)	0.7278 (0.2070)	1.2146 (0.1084)
30.0	0.667	1.4418 (0.1613)	0.9341 (0.0586)	0.7431 (0.1643)	1.2259 (0.1034)
30.0	0.750	1.2372 (0.1945)	0.9945 (0.0601)	0.6689 (0.1763)	1.3157 (0.1088)
30.0	0.833	1.1567 (0.1768)	1.0043 (0.0634)	0.6347 (0.1415)	1.2311 (0.1046)
50.0	0.100	2.7073 (0.3164)	1.2462 (0.1022)	0.4994 (0.0885)	1.1987 (0.0911)
50.0	0.200	6.8685 (0.6027)	1.7598 (0.0962)	1.1281 (0.1485)	1.6567 (0.1095)
50.0	0.300	3.0675 (0.4068)	2.1329 (0.1391)	0.9577 (0.1325)	1.5342 (0.1035)
50.0	0.400	3.8674 (0.4917)	2.1284 (0.1276)	1.2024 (0.1555)	1.4429 (0.1071)
50.0	0.500	3.1833 (0.3945)	1.9306 (0.1351)	1.1686 (0.1572)	1.3833 (0.0962)
50.0	0.600	3.9203 (0.5356)	1.9306 (0.1351)	1.1592 (0.1657)	1.3686 (0.1136)
50.0	0.700	3.2193 (0.3764)	1.8847 (0.1192)	1.2059 (0.1847)	1.3282 (0.1233)
50.0	0.800	4.0614 (0.4772)	1.9755 (0.1284)	1.2879 (0.2084)	1.6455 (0.1211)
50.0	0.900	6.3063 (0.6415)	2.6817 (0.1576)	1.5957 (0.2244)	1.8842 (0.1176)

Table B.1. HDNS results of Γ (in $\mathrm{cm}^3\,\mathrm{s}^{-1}$) of cross-size collisions for different Taylor microscale Reynolds number R_λ, and turbulent dissipation rate ϵ. The values between parentheses are the corresponding statistical uncertainties ($\pm$ one standard deviation).

		R_λ			
		43.0		72.4	
a_1	a_2/a_1	ϵ ($\mathrm{cm}^2\,\mathrm{s}^{-3}$)		ϵ ($\mathrm{cm}^2\,\mathrm{s}^{-3}$)	
(μm)		100.0	400.0	100.0	400.00
20.0	0.250	1.5517E-06 (1.2972E-07)	2.2900E-06 (1.9503E-07)	1.9045E-06 (2.3763E-07)	2.4309E-06 (2.4829E-07)
20.0	0.375	7.5270E-06 (3.4858E-07)	1.1287E-05 (5.6638E-07)	8.8719E-06 (5.5936E-07)	9.9230E-06 (6.1624E-07)
20.0	0.500	1.5462E-05 (5.8712E-07)	2.0276E-05 (8.1588E-07)	1.5992E-05 (1.2622E-06)	1.8808E-05 (9.3821E-07)
20.0	0.600	1.6479E-05 (8.2550E-07)	2.5000E-05 (7.7108E-07)	1.8951E-05 (1.0161E-06)	2.4417E-05 (1.0367E-06)
20.0	0.700	1.3101E-05 (7.4180E-07)	2.1702E-05 (6.8854E-07)	1.4263E-05 (7.2393E-07)	2.2727E-05 (9.7505E-07)
20.0	0.800	8.9612E-06 (3.0917E-07)	1.7098E-05 (5.1566E-07)	9.1716E-06 (5.6981E-07)	1.6770E-05 (7.2316E-07)
20.0	0.900	3.2814E-06 (1.5493E-07)	1.1629E-05 (4.1115E-07)	3.1307E-06 (1.9665E-07)	1.0320E-05 (4.9801E-07)
30.0	0.167	1.9429E-05 (1.5291E-06)	1.9011E-05 (2.7516E-06)	2.0273E-05 (1.6714E-06)	2.6299E-05 (2.5494E-06)
30.0	0.250	1.7834E-04 (2.4218E-06)	1.3346E-04 (6.1993E-06)	1.1525E-04 (4.4910E-06)	1.3876E-04 (4.1066E-06)
30.0	0.333	2.0555E-04 (3.0194E-06)	2.4086E-04 (4.3127E-06)	2.1461E-04 (1.1187E-05)	2.4272E-04 (4.7629E-06)
30.0	0.417	2.6110E-04 (3.7185E-06)	3.2031E-04 (4.7030E-06)	2.6778E-04 (9.8890E-06)	3.0597E-04 (6.3640E-06)
30.0	0.500	3.0080E-04 (4.8359E-06)	3.6024E-04 (5.4008E-06)	3.0391E-04 (6.9400E-06)	3.8215E-04 (5.9947E-06)
30.0	0.583	3.1576E-04 (4.4638E-06)	4.0216E-04 (5.0970E-06)	3.1192E-04 (9.6954E-06)	4.1120E-04 (7.9194E-06)
30.0	0.667	3.3778E-04 (1.9132E-06)	4.0045E-04 (5.5581E-06)	3.0867E-04 (4.7471E-06)	3.9667E-04 (6.4504E-06)
30.0	0.750	2.5176E-04 (3.8124E-06)	3.7126E-04 (5.7159E-06)	2.5234E-04 (7.4679E-06)	4.0105E-04 (7.6133E-06)
30.0	0.833	1.7545E-04 (3.3032E-06)	3.1058E-04 (5.2732E-06)	1.7890E-04 (4.3496E-06)	3.1913E-04 (6.3427E-06)
50.0	0.100	5.1164E-04 (1.4366E-05)	3.2395E-04 (1.2308E-05)	5.3216E-04 (2.0248E-05)	6.0538E-04 (2.5331E-05)
50.0	0.200	2.1836E-03 (1.5667E-05)	2.3361E-03 (2.7039E-05)	2.0880E-03 (3.5339E-05)	2.3334E-03 (3.6225E-05)
50.0	0.300	3.1762E-03 (5.5161E-05)	3.2621E-03 (4.9463E-05)	2.9914E-03 (3.8707E-05)	3.3451E-03 (4.3925E-05)
50.0	0.400	3.6972E-03 (4.5674E-05)	4.0195E-03 (5.0979E-05)	3.5868E-03 (4.6826E-05)	3.9142E-03 (5.8356E-05)
50.0	0.500	3.9749E-03 (5.5525E-05)	4.2574E-03 (6.9693E-05)	3.9015E-03 (4.8645E-05)	4.0661E-03 (5.9720E-05)
50.0	0.600	3.9947E-03 (3.4402E-05)	4.6809E-03 (3.4402E-05)	3.8214E-03 (6.1408E-05)	4.2576E-03 (6.9557E-05)
50.0	0.700	3.4838E-03 (6.5189E-05)	3.9504E-03 (5.8345E-05)	3.5831E-03 (6.2396E-05)	3.9532E-03 (7.4952E-05)
50.0	0.800	2.8550E-03 (3.8072E-05)	3.3643E-03 (4.7422E-05)	2.7776E-03 (6.6310E-05)	3.4554E-03 (5.9016E-05)
50.0	0.900	1.8395E-03 (2.6076E-05)	2.5709E-03 (3.4452E-05)	1.7736E-03 (4.4267E-05)	2.4071E-03 (4.0650E-05)

Table B.2. HDNS results of $\langle |w_r| \rangle$ (in cm s^{-1}) of cross-size collisions for different Taylor microscale Reynolds number R_λ, and turbulent dissipation rate ϵ. The values between parentheses are the corresponding statistical uncertainties ($\pm$ one standard deviation).

		R_λ			
		43.0		72.4	
a_1	a_2/a_1	ϵ (cm^2 s^{-3})		ϵ (cm^2 s^{-3})	
(μm)		100.0	400.0	100.0	400.00
20.0	0.250	0.0564 (0.0006)	0.0682 (0.0010)	0.0607 (0.0009)	0.0679 (0.0015)
20.0	0.375	0.1603 (0.0031)	0.2122 (0.0071)	0.1557 (0.0042)	0.1787 (0.0064)
20.0	0.500	0.2599 (0.0076)	0.3130 (0.0126)	0.2683 (0.0146)	0.2624 (0.0142)
20.0	0.600	0.2686 (0.0098)	0.3057 (0.0109)	0.2413 (0.0116)	0.3421 (0.0158)
20.0	0.700	0.1801 (0.0069)	0.2379 (0.0096)	0.1751 (0.0068)	0.2587 (0.0146)
20.0	0.800	0.0967 (0.0023)	0.1485 (0.0046)	0.0975 (0.0042)	0.1398 (0.0058)
20.0	0.900	0.0378 (0.0008)	0.0894 (0.0025)	0.0327 (0.0009)	0.0679 (0.0022)
30.0	0.167	0.1959 (0.0050)	0.2474 (0.0185)	0.2159 (0.0061)	0.3048 (0.0182)
30.0	0.250	1.9427 (0.0483)	1.4045 (0.0798)	1.1674 (0.0454)	1.4817 (0.0549)
30.0	0.333	2.0323 (0.0406)	2.1695 (0.0871)	1.8642 (0.2378)	2.0808 (0.0732)
30.0	0.417	2.2641 (0.0645)	2.6129 (0.0839)	2.4169 (0.1522)	2.5535 (0.1112)
30.0	0.500	2.2692 (0.1031)	2.8490 (0.1764)	2.4565 (0.1256)	2.6497 (0.1234)
30.0	0.583	2.1932 (0.0690)	2.6617 (0.1575)	2.2162 (0.1589)	2.7127 (0.1181)
30.0	0.667	2.1360 (0.0026)	2.1585 (0.1228)	1.8598 (0.0822)	2.2317 (0.0834)
30.0	0.750	1.4097 (0.0544)	1.7734 (0.1037)	1.3340 (0.0969)	1.8104 (0.0727)
30.0	0.833	0.8343 (0.0320)	1.0421 (0.0064)	0.8149 (0.0318)	1.2360 (0.0475)
50.0	0.100	2.2223 (0.0548)	1.3832 (0.0500)	2.2418 (0.0780)	2.1455 (0.0807)
50.0	0.200	9.1425 (0.2589)	9.7019 (0.2110)	9.9111 (0.6374)	9.9902 (0.4291)
50.0	0.300	11.5087 (0.8125)	11.8393 (0.7027)	11.4135 (0.5668)	11.2931 (0.6952)
50.0	0.400	11.0997 (0.6942)	12.2919 (0.6254)	11.9734 (0.8319)	10.8482 (0.6868)
50.0	0.500	10.2335 (0.7940)	10.3972 (0.6247)	12.5237 (0.6776)	12.3409 (0.6934)
50.0	0.600	9.8487 (0.4472)	9.8487 (0.9472)	9.6311 (0.6643)	10.7453 (0.6192)
50.0	0.700	8.6905 (0.5326)	8.2768 (0.3706)	6.8121 (0.5147)	8.8474 (0.6564)
50.0	0.800	5.2532 (0.2769)	5.5974 (0.2313)	5.1650 (0.3948)	6.1184 (0.2957)
50.0	0.900	2.7722 (0.1010)	3.1105 (0.1146)	2.2209 (0.1345)	3.026 (0.1047)

Table B.3. HDNS results of g_{12} of cross-size collisions for different Taylor microscale Reynolds number R_λ, and turbulent dissipation rate ϵ. The values between parentheses are the corresponding statistical uncertainties (± one standard deviation).

		R_λ			
		43.0		72.4	
a_1	a_2/a_1	ϵ (cm^2 s^{-3})		ϵ (cm^2 s^{-3})	
(μm)		100.0	400.0	100.0	400.00
20.0	0.250	1.3559 (0.0456)	1.6325 (0.0619)	1.4474 (0.0776)	1.6145 (0.0763)
20.0	0.375	1.2587 (0.0532)	1.3795 (0.0774)	1.5911 (0.0951)	1.5231 (0.0916)
20.0	0.500	1.1610 (0.0609)	1.3059 (0.0982)	1.1185 (0.1197)	1.4577 (0.1295)
20.0	0.600	1.1113 (0.0736)	1.3776 (0.0734)	1.3963 (0.1126)	1.1123 (0.0782)
20.0	0.700	1.2595 (0.0854)	1.3801 (0.0774)	1.3215 (0.0895)	1.2974 (0.0837)
20.0	0.800	1.4324 (0.0661)	1.5475 (0.0767)	1.3344 (0.1155)	1.6746 (0.1055)
20.0	0.900	1.3234 (0.0576)	1.6820 (0.0806)	1.4034 (0.0945)	1.8990 (0.1003)
30.0	0.167	1.8529 (0.0996)	1.5407 (0.1734)	1.6164 (0.1012)	1.5446 (0.1586)
30.0	0.250	1.0739 (0.0307)	1.1642 (0.0812)	1.1705 (0.0707)	1.1696 (0.0560)
30.0	0.333	1.0375 (0.0272)	1.1397 (0.0503)	1.0351 (0.2871)	1.1126 (0.0503)
30.0	0.417	1.0154 (0.0368)	1.0705 (0.0432)	1.1223 (0.0970)	1.2029 (0.0632)
30.0	0.500	1.0045 (0.0537)	1.0982 (0.0788)	0.9252 (0.0616)	1.1302 (0.0602)
30.0	0.583	1.0236 (0.0391)	1.0395 (0.0741)	1.0236 (0.0877)	1.0990 (0.0638)
30.0	0.667	1.0364 (0.0200)	1.0677 (0.0692)	0.9795 (0.0544)	1.2561 (0.0501)
30.0	0.750	1.0175 (0.0516)	1.3049 (0.0845)	1.0070 (0.0845)	1.2984 (0.0578)
30.0	0.833	1.2157 (0.0524)	1.4036 (0.0784)	1.1323 (0.0631)	1.4816 (0.0661)
50.0	0.100	1.2783 (0.0514)	1.3092 (0.0539)	1.2941 (0.0758)	1.4725 (0.0856)
50.0	0.200	1.0501 (0.0392)	1.0880 (0.0342)	0.9931 (0.0939)	1.0244 (0.0593)
50.0	0.300	1.0575 (0.0933)	1.1172 (0.0816)	1.0431 (0.0743)	0.9524 (0.0719)
50.0	0.400	1.0472 (0.0744)	1.0425 (0.0724)	0.8482 (0.0814)	1.0006 (0.0733)
50.0	0.500	1.1396 (0.1105)	1.1194 (0.0848)	1.1190 (0.0965)	1.0696 (0.0785)
50.0	0.600	0.9889 (0.0686)	1.1420 (0.1131)	0.9538 (0.0846)	1.1036 (0.0959)
50.0	0.700	1.1920 (0.1330)	1.1838 (0.0681)	1.1114 (0.0919)	1.0400 (0.0802)
50.0	0.800	1.0537 (0.0765)	1.2066 (0.0497)	1.0626 (0.1095)	1.1072 (0.0601)
50.0	0.900	1.2381 (0.0477)	1.5080 (0.0529)	1.3167 (0.0872)	1.4182 (0.0559)

Table B.4. HDNS results of η_E of cross-size collisions for different Taylor microscale Reynolds number R_λ, and turbulent dissipation rate ϵ. The values between parentheses are the corresponding statistical uncertainties (± one standard deviation).

		R_λ			
		43.0		72.4	
a_1	a_2/a_1	ϵ (cm^2 s^{-3})		ϵ (cm^2 s^{-3})	
(μm)		100.0	400.0	100.0	400.00
20.0	0.250	1.0465 (0.1050)	1.4960 (0.1492)	1.2685 (0.1843)	1.6322 (0.2014)
20.0	0.375	1.0399 (0.0642)	1.4787 (0.0927)	1.2214 (0.1005)	1.2760 (0.1008)
20.0	0.500	1.0394 (0.0536)	1.2380 (0.0636)	1.0449 (0.1016)	1.1391 (0.0729)
20.0	0.600	0.9812 (0.0582)	1.3477 (0.0627)	1.0696 (0.0810)	1.2204 (0.0792)
20.0	0.700	0.9550 (0.0661)	1.3232 (0.0630)	1.0288 (0.0736)	1.3251 (0.0794)
20.0	0.800	1.2470 (0.0583)	1.8305 (0.0784)	1.2226 (0.0981)	1.7161 (0.0983)
20.0	0.900	1.7430 (0.1000)	4.1555 (0.2089)	1.5700 (0.1239)	3.7878 (0.3046)
30.0	0.167	1.2185 (0.1109)	1.6501 (0.1759)	1.2737 (0.1372)	1.6233 (0.1895)
30.0	0.250	1.6505 (0.0399)	1.1733 (0.0614)	1.0661 (0.0610)	1.2508 (0.0557)
30.0	0.333	1.0734 (0.0282)	1.1578 (0.0323)	1.1141 (0.0735)	1.1437 (0.0356)
30.0	0.417	1.0223 (0.0252)	1.1507 (0.0292)	1.0535 (0.0632)	1.0735 (0.0388)
30.0	0.500	1.0247 (0.0306)	1.1230 (0.0296)	0.9981 (0.0452)	1.1272 (0.0354)
30.0	0.583	1.0453 (0.0249)	1.1819 (0.0288)	1.0312 (0.0484)	1.1925 (0.0396)
30.0	0.667	1.1894 (0.0195)	1.2019 (0.0298)	1.0802 (0.0317)	1.1371 (0.0318)
30.0	0.750	1.0710 (0.0285)	1.2460 (0.0346)	1.0540 (0.0463)	1.2671 (0.0427)
30.0	0.833	1.1150 (0.0353)	1.3767 (0.0419)	1.1172 (0.0413)	1.3450 (0.0481)
50.0	0.100	1.0465 (0.0417)	1.1761 (0.0666)	1.0689 (0.0627)	1.2011 (0.0666)
50.0	0.200	1.0610 (0.0176)	1.1049 (0.0229)	1.0000 (0.0271)	1.0788 (0.0282)
50.0	0.300	1.0918 (0.0370)	1.0890 (0.0321)	1.0251 (0.0252)	1.1260 (0.0285)
50.0	0.400	1.0739 (0.0235)	1.1435 (0.0261)	1.0557 (0.0270)	1.0915 (0.0303)
50.0	0.500	1.0792 (0.0295)	1.1201 (0.0340)	1.0279 (0.0265)	1.0509 (0.0304)
50.0	0.600	1.0639 (0.0222)	1.1190 (0.0212)	1.0458 (0.0332)	1.0857 (0.0415)
50.0	0.700	1.0346 (0.0375)	1.1209 (0.0317)	1.0286 (0.0349)	1.0629 (0.0432)
50.0	0.800	1.0326 (0.0287)	1.0982 (0.0291)	1.0210 (0.0481)	1.1027 (0.0453)
50.0	0.900	1.1904 (0.0307)	1.2629 (0.0340)	1.0877 (0.0469)	1.1158 (0.0351)

To estimate the disturbance flow $u_3^{(k)}$ felt by a droplet, we consider only two isolated droplets falling along a single vertical line, with the a_1-droplet approaching the a_2-droplet from above. In this case, using Stokes disturbance flow and the improved superposition method [27] we can determine the disturbance flow felt by each droplet from the following coupled equations

$$u_3^{(1)} = \left[\frac{3}{2}\frac{a_2}{z} - \frac{1}{2}\left(\frac{a_2}{z}\right)^3\right](v_{p2}^* - u_3^{(2)}), \tag{C.4}$$

$$u_3^{(2)} = \left[\frac{3}{2}\frac{a_1}{z} - \frac{1}{2}\left(\frac{a_1}{z}\right)^3\right](v_{p1}^* - u_3^{(1)}), \tag{C.5}$$

where z is the distance between the two droplets ($z = -(v_{p1}^* - v_{p2}^*)\tau + R$). Solving for $u_3^{(1)}$ and $u_3^{(2)}$ we obtain

$$u_3^{(1)} = \frac{h_2(v_{p2}^* - h_1 v_{p1}^*)}{1 - h_1 h_2}, \tag{C.6}$$

$$u_3^{(2)} = \frac{h_1(v_{p1}^* - h_2 v_{p2}^*)}{1 - h_1 h_2}, \tag{C.7}$$

where h_i is given by

$$h_i = \frac{3}{2}\frac{a_i}{z} - \frac{1}{2}\left(\frac{a_i}{z}\right)^3.$$

Introducing equations (C.6) and (C.7) into (C.3), we obtain a set of coupled integral equations

$$v_{p1}^*(\tau = 0) \approx \frac{1}{\tau_{p1}}\int_{-\infty}^{0} \frac{h_2(\tau)(v_{p2}^*(\tau) - h_1(\tau)(v_{p1}^*(\tau))}{1 - h_1(\tau)h_2(\tau)} \exp\left(\frac{\tau}{\tau_{p1}}\right) \mathrm{d}\tau + v_{p_1}, \tag{C.8}$$

$$v_{p2}^*(\tau = 0) \approx \frac{1}{\tau_{p2}}\int_{-\infty}^{0} \frac{h_1(\tau)(v_{p1}^* - h_2(\tau)v_{p2}^*(\tau))}{1 - h_1(\tau)h_2(\tau)} \exp\left(\frac{\tau}{\tau_{p2}}\right) \mathrm{d}\tau + v_{p_2}. \tag{C.9}$$

An equivalent representation is the following set of 1D equations of motion

$$\frac{\mathrm{d}v_{p1}^*}{\mathrm{d}t} = \frac{u_3^{(1)} - v_{p1}^* + v_{p_1}}{\tau_{p_1}}, \tag{C.10}$$

$$\frac{\mathrm{d}v_{p2}^*}{\mathrm{d}t} = \frac{u_3^{(2)} - v_{p2}^* + v_{p_2}}{\tau_{p_2}}, \tag{C.11}$$

with the initial conditions $v_{p1}^*(\tau \to -\infty) = v_{p1}$ and $v_{p2}^*(\tau \to -\infty) = v_{p2}$. We solve for v_{p1} and v_{p2} at contact numerically by integrating (C.10) and (C.11) starting from a large separation z at $100(a_1 + a_2)$. The location and velocity of each droplet were advanced using a fourth-order Adams–Bashforth method until the a_1-droplet captures the a_2-droplet.

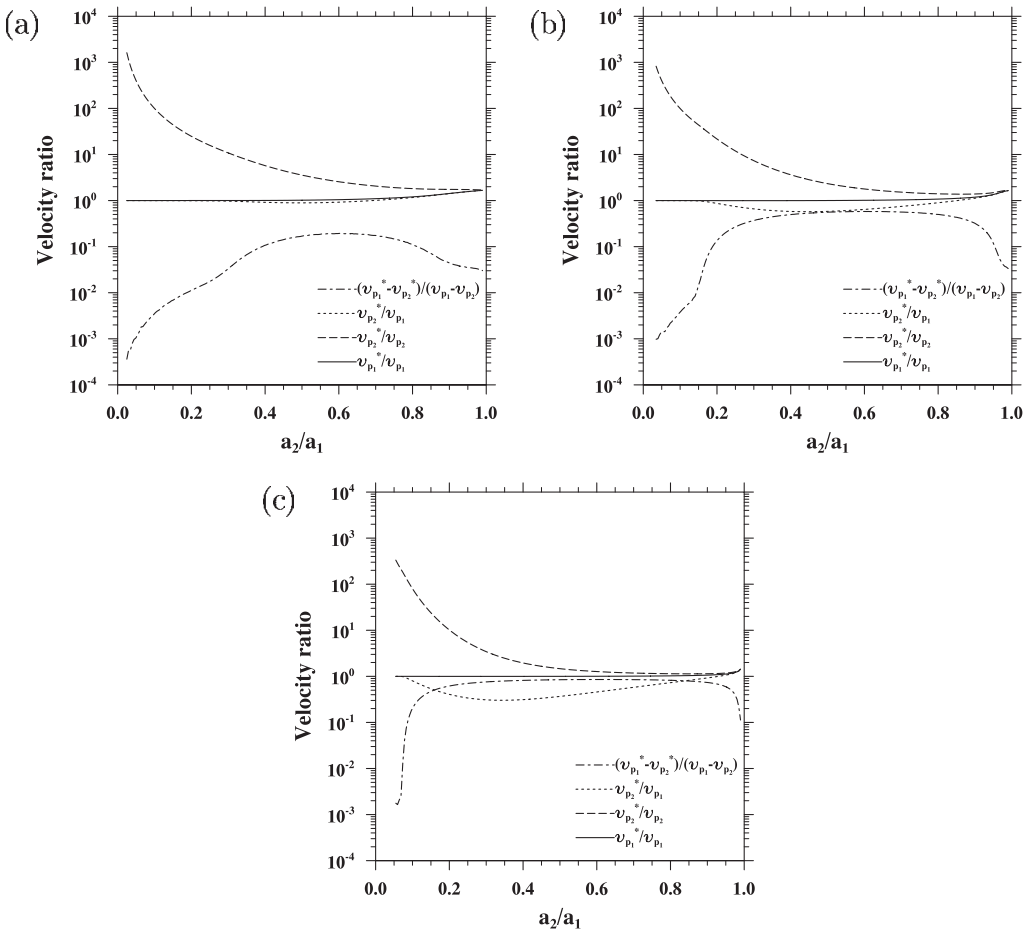

Figure C.1. Ratio of the modified terminal velocities to the original terminal velocities. (a) $a_1 = 20\,\mu$m, (b) $a_1 = 30\,\mu$m and (c) $a_1 = 50\,\mu$m.

The computed vertical droplet velocities at the time of capture are shown in figure C.1. Several important observations can be made. First, both the collecting droplet and the collected droplet settle faster than their respective terminal velocity due to the disturbance flow. For $a_2/a_1 \leqslant 0.5$, the increase in the velocity of the collecting droplet can be neglected such that $v_{p1}^* \approx v_{p1}$ and $u_3^{(1)} \approx 0$. Then the velocity of the smaller droplet can be approximated, using equation (C.9), as

$$v_{p2}^*(\tau = 0) \approx v_{p2} + v_{p1} \int_0^\infty \left[\frac{1.5a_1}{R + (v_{p1} - v_{p2}^*)\tau_{p2} s} - 0.5 \left(\frac{a_1}{R + (v_{p1} - v_{p2}^*)\tau_{p2} s} \right)^3 \right] \exp(-s)\mathrm{d}s. \tag{C.12}$$

Furthermore, figure C.1 shows that $v_{p2}^* \to v_{p1}$ as $a_2/a_1 \to 0$. As a leading-order approximation, we may set $v_{p1} - v_{p2}^* = 0$ in the integrand of equation (C.12) and obtain the following asymptotic expression for $v_{p2}^*(\tau = 0)$ at small $\varrho \equiv a_2/a_1$

$$\frac{v_{p2}^*(\tau = 0)}{v_{p2}} = 1 + \frac{1}{\varrho^2} \left[\frac{1.5}{1 + \varrho} - \frac{0.5}{(1 + \varrho)^3} \right]. \tag{C.13}$$

The above approximation explains why $v_{p2}^*(\tau=0)/v_{p2}$ depends mainly on the size ratio ϱ, as shown by the curves for $v_{p2}^*(\tau=0)/v_{p2}$ for three different a_1 values. Quantitatively, equation (C.13) yields $v_{p2}^*(\tau=0)/v_{p2}=99.8$ at $\varrho=0.1$, a value close to what is shown in figure C.1. Equation (C.13) also implies that

$$\frac{v_{p2}^*(\tau=0)}{v_{p1}} \approx 1-0.5\varrho^2 \quad \text{and} \quad v_{p1}^*-v_{p2}^* \approx 0.5\varrho^2, \tag{C.14}$$

as $\varrho \to 0$. Therefore, the relative velocity is very small in the limit of $a_2/a_1 \to 0$ due to HI.

In the opposite limit of $a_2/a_1 \to 1$, we can write

$$v_{p1}^*(\tau=0)=v_{p2}^*(\tau=0) \approx v_p+\frac{1}{\tau_{\mathrm{p}}}\int_{-\infty}^{0}\frac{h(1-h)v_{p1}^*}{1-h^2}\exp(\tau/\tau_p)\mathrm{d}\tau. \tag{C.15}$$

Approximating the integrand excluding the exponential term by the value at $\tau=0$ (i.e. $h=11/16$ and $v_p^*(\tau)=v_p^*(0)$), we obtain

$$v_{p1}^*=v_{p2}^* \approx \tfrac{27}{16}v_p=1.6875v_p. \tag{C.16}$$

This is close to the value shown in figure C.1 (1.666 for $a_1=20\,\mu$m, 1.648 for $a_1=30\,\mu$m and 1.411 $a_1=50\,\mu$m).

The second observation is that $(v_{p1}^*-v_{p2}^*)$ is always less than $(v_{p1}-v_{p2})$, indicating that the radial relative velocity is always reduced due to HI. The normalized ratio $(v_{p1}^*-v_{p2}^*)/(v_{p1}-v_{p2})$ decreases with a_1 for a given a_2/a_1 ratio, since both droplets become more responsive to the disturbance flow.

Finally, for a given a_1, figure C.1 shows that there is a maximum normalized relative motion at an intermediate value of the a_2/a_1 ratio.

References

[1] Arenberg D 1939 *Bull. Am. Meteorol. Soc.* **20** 444–5
[2] Sudaram S and Collins L R 1997 *J. Fluid Mech.* **75** 337–50
[3] Wang L-P, Wexler A and Zhou Y 2000 *J. Fluid Mech.* **415** 117–53
[4] Zhou Y, Wexler A and Wang L-P 2001 *J. Fluid Mech.* **433** 77–104
[5] Wang L-P, Ayala O, Kasprzak S E and Grabowski W W 2005 *J. Atmos. Sci.* **62** 2433–50
[6] Ayala O, Wang L-P and Grabowski W W 2007 *J. Comput. Phys.* **225** 51–73
[7] Pinsky M B and Khain A P 1997 *J. Aerosol Sci.* **28** 1177–214
[8] de Almeida F C 1979 *J. Atmos. Sci.* **36** 1564–76
[9] Grover S N and Pruppacher H R 1985 *J. Atmos. Sci.* **42** 2305–18
[10] Koziol A S and Leighton H G 1996 *J. Atmos. Sci.* **53** 1910–20
[11] Pinsky M B, Khain A P and Shapiro M 1999 *J. Atmos. Sci.* **56** 2585–600
[12] Franklin C N, Vaillancourt P A, Yau M K and Bartello P 2005 *J. Atmos. Sci.* **62** 2451–66
[13] Wang L-P, Ayala O and Grabowski W W 2007 *J. Turbul.* **8** N25 doi: 10.1080/14685240701233426
[14] Franklin C N, Vaillancourt P A and Yau M K 2007 *J. Atmos. Sci.* **64** 938–54
[15] Ayala O, Rosa B, Wang L-P and Grabowski W W 2008 Effects of turbulence on the geometric collision rate of sedimenting droplets: Part 1. Results from direct numerical simulation *New J. Phys.* **10** 075015
[16] Ayala O, Rosa B, Wang L-P and Grabowski W W 2008 Effects of turbulence on the geometric collision rate of sedimenting droplets: Part 2. Theory and parameterization. *New J. Phys.* **10** 075016
[17] Kim S and Karrila S J 1991 *Microhydrodynamics, Principles and Selected Applications* (Boston, MA: Butterworth-Heinemann) p 507
[18] Noh Y and Fernando H J S 1993 *Phys. Fluids* **5** 3049–55

[19] Wang L-P and Maxey M R 1993 *J. Fluid Mech.* **27** 27–68
[20] Allen M P and Tildesley D J 1987 *Computer Simulation of Liquids* (New York: Oxford University Press) p 408
[21] Batchelor G K 1972 *J. Fluid Mech.* **52** 245–68
[22] Wang L-P, Ayala O and Xue Y 2005 *Phys. Fluids* **17** 067103
[23] Rogers R R and Yau M K 1989 *A Short Course in Cloud Physics* (New York: Pergamon) p 293
[24] Pruppacher H R and Klett J D 1997 *Microphysics of Clouds and Precipitation* (Dordrecht: Kluvert) p 954
[25] Pinsky M, Khain A and Krugliak H 2008 *J. Atmos. Sci.* **65** 357–74
[26] Pinsky M, Khain A P and Shapiro M 2001 *J. Atmos. Sci.* **58** 742–64
[27] Davila J and Hunt J C R 2001 *J. Fluid Mech.* **440** 117–45
[28] Wang L-P, Ayala O and Grabowski W W 2005 *J. Atmos. Sci.* **62** 1255–66
[29] Xue Y, Wang L-P and Grabowski W W 2007 *J. Atmos. Sci.* **65** 331–56
[30] Maxey M R 1987 *J. Fluid Mech.* **174** 441–65
[31] Rosa B, Wang L-P and Grabowski W W 2007 *Proc. 6th Int. Conf. on Multiphase Flow (Leipzig)*
[32] Khain A, Pinsky M, Elperin T, Kleeorin N, Rogachevski I and Kostinski A 2007 *Atmos. Res.* **86** 1–20
[33] Reeks M W 1977 *J. Fluid Mech.* **83** 529–46